Politecnico di Torino
Dottorato in Dispositivi Elettronici

Ph.D. Thesis

Developement of simulation tools for the analysis of variability in advanced semiconductor electron devices

Tutor:
Prof. Fabrizio Bonani
Prof. Simona Donati Guerrieri

Candidate:
Riccardo Tisseur

Acknowledgements

First of all I want to thank Prof. Simona Donati Guerrieri for his patience supervision and immense help during all the three year of doctorate. I admire his huge knowledge and mastery on the device physics.
A special thank to Fabio Lorenza Traversa for his help on the use of the meshgenerator tools and for the patience supervision during my period in Spain.
I thank all the other members of the laboratory who has helped me during these three years. I'm grateful at Michele Goano and Francesco Bertazzi for the help in the use of server machine and Synopsis tools.
I want to thank my wife for her unconditional support and my family for their constant presence in my life. Without my wife, my family and my friends nothing of what I have done has ever been possible.

Contents

Chapter 1

Background and motivation

The demand for electron devices with higher performances is growing at high rate. One of the main causes is the success of portable devices like tablet and smart-phones which has enhanced the request of high performances with low consumption. This request can be translated into technology scaling because smaller devices need lower voltages supply, leading to lower consumption and higher speed, and high reliability .

The progressive down-scaling has been the driving force behind the integrated circuit (IC) industry for several decades, continuously delivering higher component densities and greater chip functionality, while reducing the cost per function from one CMOS technology generation to the next. Moore's law boosts IC industry profits by constantly releasing high-quality and inexpensive electronic applications into the market using new technologies. From the 1 μm gate lengths of the eighties to the 35 nm gate lengths of contemporary 22 nm technology, the industry successfully achieved its scaling goals, not only miniaturizing devices but also improving device performance.

However, the years of *happy scaling* are over. Several challenges are facing the further miniaturization of the transistors in Si chips. First, there are the process challenges of continued scaling including, among others, sub-wavelength patterning and the formation of ultra-shallow junctions. Continual process innovation is needed, including immersion optical lithography, and the flash lamp and laser annealing implemented from the 45 nm CMOS technology to achieve high-fidelity patterns and high-activation/low dopant diffusion. Secondly, the scaling of contemporary deep-decananometer gate length transistors results in the deterioration of electrical characteristics due to short-channel, quantum mechanical and transport effects. Countermeasures like halo-doping can suppress the short-channel effect in conventional MOSFETs but at the expense of increased quantum effects and reduced mobility. Novel MOSFET structures such as fully-depleted silicon-on-insulator or or 3D (FINFET) FETs devices are required to achieve a fundamental improvement in electrostatic integrity. Finally, intrinsic parameter fluctuations, resulting from the discreteness of charge and the granular nature of matter in real decanano devices, hamper the integration of scaled transistors. Statistical variability unavoidably increases drastically with further scaling. It requires the introduction of novel device architectures and the adaptation of smarter circuit and system design strategies.

In order to achieve these results, not only the silicon industry, but also emerging technologies, have to optimize the process and to investigate deeply the physical limitations. Physical simulations have an important role in the reduction of the number of trials and errors during the development of new products, reducing thus the time and the cost of new device development. Starting from the material characteristics to the final circuit, simulations are used to study complex systems and investigate new way of optimization [1].

1.1 Scaling trends

The scaling of the MOSFET devices has continued from its first introduction in integrated circuits four decades ago. This has resulted in doubling the components density on a single chip by proportionally scaling of the transistor dimensions over a period of time, this scaling trend following the famous Moore's law [2]. The scaling directly improves performance while controlling the power consumption by reducing the supply voltage and carefully tuning the design.

Figure 1.1 shows a MOSFET draft which consists of two back-to-back connected p-n junctions. The gate voltage applied across metal-oxide-semiconductor (MOS) capacitor creates an inversion channel connecting the source and the drain, and controls the carrier density in it. The MOSFET has two critical structural parameters from an operational point of view, namely gate length and gate dielectric thickness. MOSFET scaling affects both lateral, the gate length, and vertical, the oxide thickness, device dimensions. While the reduction of the lateral dimensions increases the transistor density in a chip, the reduction of the oxide thickness is needed to ensure good electrostatic integrity.

1.1.1 Transistor dimensions

At each new tecnology generation, the bulk MOSFET area is reduced of one half, that means a lateral scaling of a factor $1/\sqrt{2}$, doubling the circuit density and enhancing

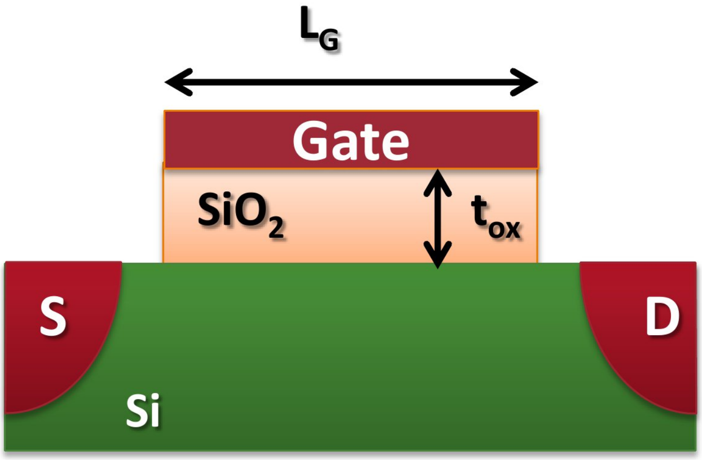

Figure 1.1: Schematic MOS representation
The MOSFET has two critical structural parameters from an operational point of view, namely gate length Lg and gate dielectric thickness tox

functionality. In contemporary MOSFETs the drain current Id is determined by

$$\frac{Id}{W} = C_{OX}(Vg - V_{th})\nu \tag{1.1}$$

where W is the channel width, C_{OX} is the gate capacitance per unit area, and ν is the source end carrier velocity. The saturation transconductance gm may be obtained by

$$\frac{gm}{W} = \frac{\partial Id}{\partial Vg}\frac{1}{W} = \frac{\varepsilon_{ox}}{t_{ox}}\nu \tag{1.2}$$

where ε_{ox} is the oxide permittivity. The carrier velocity is usually saturated in short-channel MOSFETs, thus gm/W is an index of gate oxide thickness t_{ox}. Device current and saturation transconductance are closely related to oxide thickness by the capacitance C_{ox} which is inversely proportional to oxide thickness.

1.1.2 Voltage scaling

As illustrated in Figure 1.2 the supply voltage has been continuously reduced with the advance of CMOS technology. In addition, the threshold voltage has also been reduced to maintain appropriate gate voltage overdrive. However, the reduction of supply voltage and threshold voltage has lagged the gate length and gate dielectric thickness scaling. The slower reduction of the threshold voltage is due to a combination of factors including increasing channel doping needed to control short-channel effects.

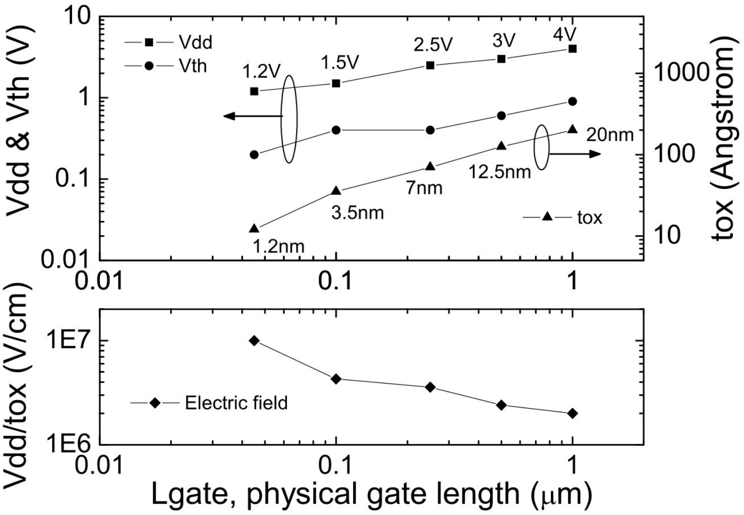

Figure 1.2: Voltage scaling trend

Supply voltage Vdd, threshold voltage V_{th}, gate oxide thickness tox and gate length Lg scaled down toghether. Gate electric field increased rapidly.

The sub-linear threshold voltage scaling in turn has retarded the scaling of the supply voltage.

1.1.3 Doping scaling

With device scaling the MOSFET substrate doping increase and it has reached more than 2×10^{18} cm^{-3} in contemporary 32 nm gate length MOSFET. In addition to the average increase of the channel doping, the design of the vertical doping profile has also changed. Retrograde doping has been introduced to short channel devices to control short-channel effects and to achieve simultaneously low threshold voltage and elevate mobility by reducing impurity scattering [3]. Short channel effect are reduced with Halo doping that blocks lateral field penetration from source and drain without affecting adversely the threshold voltage [4].

At source and drain regions structure modification have been made, e.g. lightly doped drain and shallow extensions. Lightly doped drain LDD was introduced to alleviate reliability concerns during the 5 V supply voltage period where impact ionization effect where caused by high field near the drain junction. Shallow source/drain extensions have been introduced to manage short-channel effects in successive technologies reducing the coupling between the drain voltage and the carrier concentration in the channel.

1.1.4 Nowadays MOSFET scaling

Further advancement of the MOSFET technology becomes complicated, as gate length enters within sub-100 nm nanometer regime at the 130nm technology generation, a commonly accepted critical dimension for nanoelectronics. At such dimensions, performance deterioration issues associated with transport property limitations of Si started to emerge. From the technological point of view imaging and patterning has become extremely challenging. As optical lithography is the 'work horse' of the semiconductor sector, sub-wavelength patterning is pushed to adopt resolution enhancement techniques (RET), such as optical proximity correction (OPC), to print finer lines and increase fidelity of pattern transfer [18]. Due to extreme oxide thickness scaling, the gate oxide direct tunnelling through oxides thinner than 2 nm started to dominate the gate leakage, and poses a challenge for further gate oxide scaling. Simultaneously intrinsic parameter fluctuations due to the discreteness of charge and matter, including random discrete dopants, line edge roughness, and poly-silicon granularity, introduce statistical variability in the electrical characteristics of nanoscale MOSFETs, influencing device performance and circuit yield [7].

1.2 Variability

In contemporary MOSFETs with sub-50 nm channel length, the number of dopants in the active area depleted region is of the order of a hundred, and the number of interface traps is of order of ten. The exact number and location of the discrete dopants and traps fluctuate from device to device. In addition, resist-defined gate line edge roughness is unavoidable. The gate material granularity and the oxide thickness fluctuation of 1 interatomic layer of the Si crystal lattice, also contribute to the microscopic differences in devices with identical macroscopic parameters. These microscopic fluctuations originate either from uncontrollable process aspects or from intrinsic material granularity. All these factors result in uncontrollable statistical variations in the electrical characteristics of nominally identical devices. Therefore, the characteristics of an idealised uniform transistor lose their representative meaning. Instead, a statistically significant ensemble of device characteristics has to be obtained to aid the design of circuits and systems, based on devices with statistical variability in mind.
In 1962 Shockley analysed random fluctuations in junction breakdown [5] . Its concept was extended to MOS devices by Keyes who modelled the effect of fluctuation in the number of impurity dopant in the depletion layer of a FET [6] . Process variation has

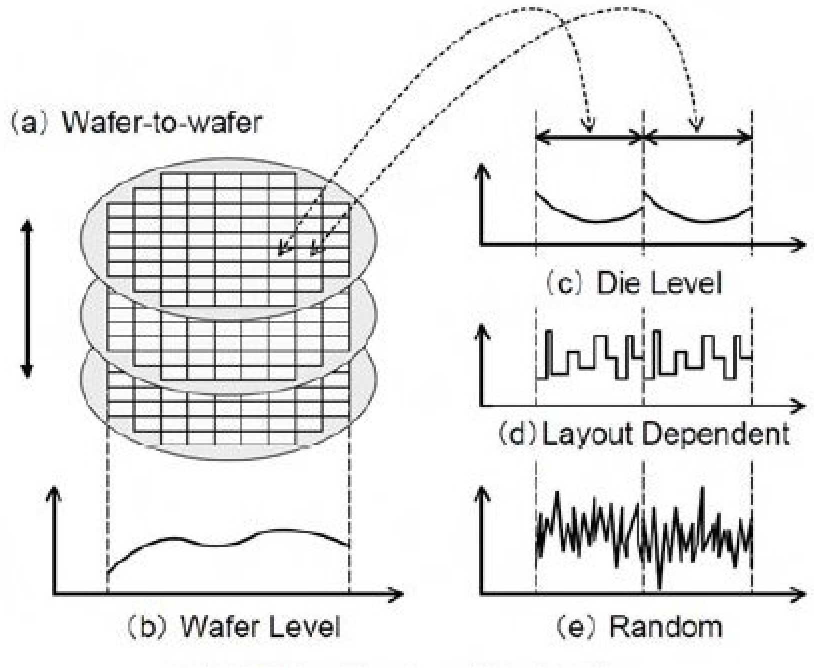

Figure 1.3: A schematic representation of Variability classification [9]
Variability can be classified by its correlation between multiple transistor placed at different positions. This figure classify the following variations: (a) Wafer-to-wafer, (b) Wafer level, (c) Die level, (d) Layout dependent and (e) random variations.

been a continuing active research field throughout semiconductor history, but now, the continuing decreasing of feature sizes to atomic dimensions and light wavelengths, suggests that the variation management will play a significant role in future technology scaling.

The miniaturization process is attracting more attention on variability sources [7]. With the device scaling and the high reliability request, new sources of variations are becoming more important, since small perturbations increase in relevance as the devices are scaled.
Variability is usually classified by its correlation between multiple transistor placed at different positions and Fig. 1.3 is a schematic representation of this classification. The following five categories can be identified:

a Wafer to Wafer variation: a possible cause is variation in the machine conditions along time of the manufacturing apparatus.

b Wafer level variation: possibles causes may be search in on-wafer process variation, gas flow etc..

c Die level variation: typically from lithography steps, because pattern exposure is performed die-by-die. It may be caused either by imperfection in reticles or non-ideality in lens systems.

d Layout dependent: variation exhibits spatial periodicity, as does die level variations, but is different in that it is strongly correlated with the specific layout of patterns, such as density, distance from the neighbouring patterns, etc. Existence of nearby patterns may affect final transistor shapes during lithography (optical proximity effect) and etching (micro loading effect). Pattern dependence of mechanical stress and annealing temperature may be also responsible.

e Random Fluctuation: is the kind of variability that exhibits no spatial correlation. The absence of correlation suggests that it is caused by some microscopic perturbations, such as random placement of discrete charges, atomic scale irregularity of gate dielectrics, and so on. Since the change of FET characteristics caused by a fixed amount of perturbation increases (i.e. sensitivity increases) as the FET size is reduced, random fluctuation rapidly increases as FETs are shrunk, which may result in failure of further scaling down of integrated circuits.

Categories (a) and (b) have always been a concern in circuit manufacturing, while the others are becoming more relevant as the miniaturization continue. Reduced device dimensions increase device sensitivity to any perturbation, while reduced supply voltages suffer of larger impact for the same amount of variation with respect to the same at higher voltages.

Furthermore, the wavelength widely used for lithography is 193 nm, which is much larger than the minimum feature sizes of state-of-the art LSIs (Large Scale Integration refer to chip with thousands of transistors). This results in increased die level and layout dependent variability of exposed pattern shapes. Though this can be, in part, offset by resolution enhancement techniques (RET) and mask data handling called optical proximity correction (OPC), layout dependence will remain to some extent. The use of mechanical stress to enhance drive performance of FETs increase layout dependence. New fabrication techniques like short thermal annealing time to reduce impurity diffusion results in non equilibrium heating, a long time of annealing as the consequence of a higher thermal uniformity, of the wafer increasing variability.

From (a) to (d) variability is directly caused by process variations or non optimal design so it can be directly controlled by introducing improvement in the process and optimizing the design. However, random fluctuations (e) seem to be not controllable due to

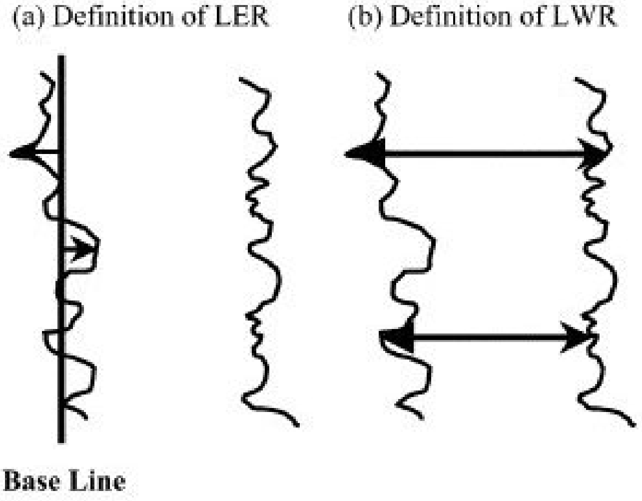

Figure 1.4: Line edge and line width roughness (LER and LWR)
A schematic representation of LER and LWR which are variations at the atomic scale of the gate line edge and width.

their microscopic origin and, for some extent, their intrinsic nature. Therefore, it is very important to quantitative understand the origins of random fluctuation. In the following paragraph we'll discuss about the main sources of random variations

1.2.1 Critical sources of random variations

Now we will briefly review the principal sources of random variations studied in the recent years [8].

Line Edge and Width roughness

Line edge and width roughness (LER and LWR) are fluctuation in the pattering line of the gate in MOS devices, see Fig.1.4 [10] . Variations in poly-gate are associated with increase in the sub threshold current as well as degradation in thethreshold voltage (VT) characteristics. LER and LWR induce fluctuations that have a strong dependence on the channel length [11] [12] and are expected to overcome the effect of RDF as devices are scaled to shorte dimensions.

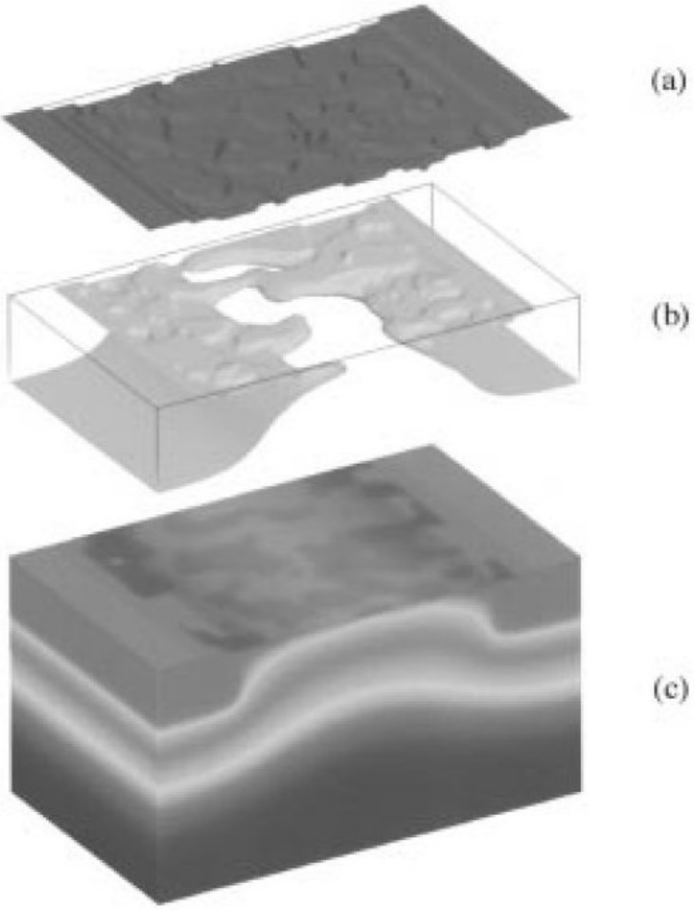

Figure 1.5: Typical profile of the random Si/SiO$_2$ interface
(a) Typical profile of the random Si/SiO$_2$ interface, (b) equiconcentration contour and (c) potential distribution

Gate Oxide variations

The reduced gate oxide thickness, also with the help of new materials like high-k dielectrics, has enhanced variations due to fluctuation of the gate dielectric. Effect of fluctuations at the atomic scale roughness of the gate interfaces has been simulated in [13], see Fig. 1.5 . Their simulations have shown that local variations of the oxide thickness induce threshold voltage variations comparable to RDF for 30 nm MOS and below. A scaling limits of 0.8 nm gate oxide thickness has been extracted in [14], where it has been shown that important threshold voltage fluctuations, due to gate-tunneling leakage current, occur when the gate oxide tunnel resistance becomes comparable to the gate poly-Si resistance.

Fixed Charge and Traps

Mobility and threshold voltage can be affected by the presence of fixed charge in the high-k layer. In [15] the authors estimated the fixed charge components in high-k stacks by varying both the SiO_2 and high-k dielectric thickness. In high-k dielectrics the presence of traps and defects induce electron mobility degradation and V_{th} instability caused by the fast transient charging by electron traps. In [16] the authors give a deep investigation of the problem to reduce the equivalent oxide thickness (1 nm EOT implies a physical thickness of 5 nm of H_fO_2) using alternative materials and pointed out the presence of defects in high-k material (the most used is H_fO_2) due to oxigen atom vacancy. It has been demonstrated that process optimization step can reduce this problem [17].

Patterning Proximity Effect

Advanced technology require aggressive lithographic and this results in pattering proximity effects, see Fig. 1.6 . To improve lithographic pattering and reduce variations OPC can be used [18]. OPC pre-distorts the mask data following specific algorithms in order to achieve a desired pattern on the wafer. OPC is based on a highly phenomenological process model that incorporates lumped optics, resist, wafer stack, and mask effects. This model generates a mask-to-wafer optical transfer function, and an OPC algorithm is written to invert the transfer function. An OPC recipe is developed using an iterative algorithm that modifies the starting database in order to achieve the desired pattern on the mask.

Chemical Mechanical Polish

Chemical mechanical polish is a critical step in device manufacturing which occur both in the front-end and back-end process. Many variations can occur in these steps, but they can be controlled improving the technique. One commonly applied method for improvement of variation in any CMP process is the addition of dummy features. In [19] the authors review some of the historical approaches to dummy-feature placement and modeling and present a time-dependent relation between post-CMP topography and layout pattern density for CMP in STI.

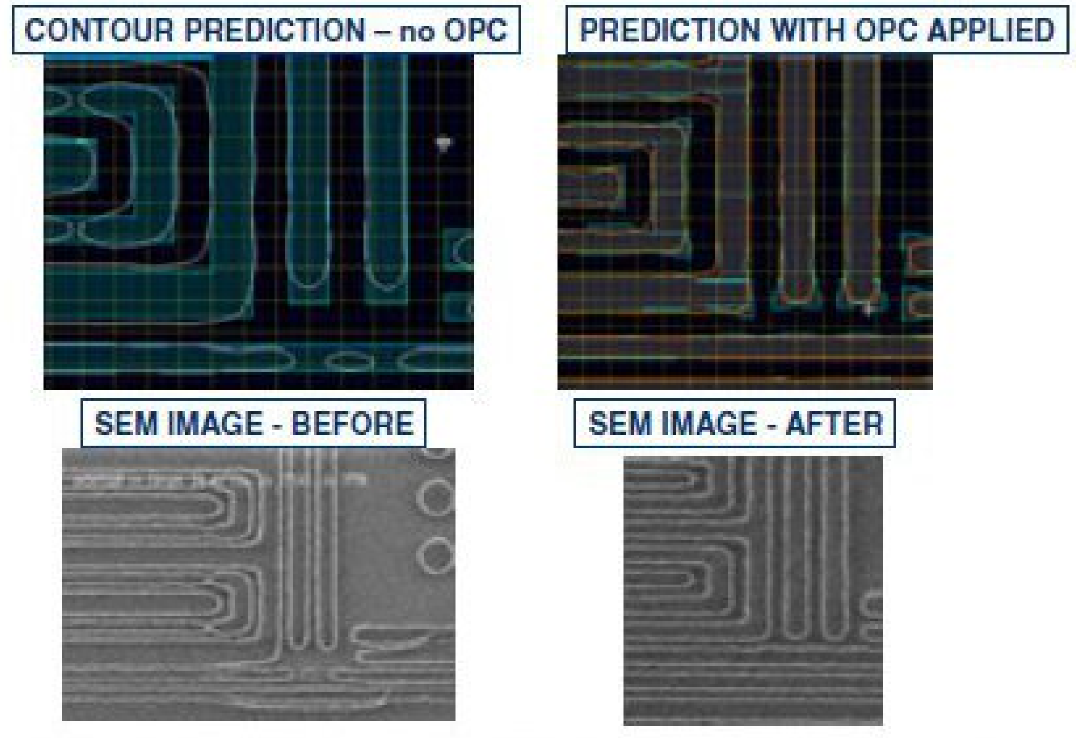

Figure 1.6: Optical proximity correction OPC
OPC pre-distorts the mask data in order to achieve a desired pattern on the wafer

Strain

During the 1980s, researchers began to explore channel strain approaches for transistor enhancement where thin Si layers were grown on relaxed SiGe substrates such that the thin Si layer would take the larger lattice constant of the SiGe and create biaxial tensile stress in the channel. In the early 2000s, a new class of transistor strain approaches was developed that used process features external to the transistor (rather than strain in the channel itself as with the biaxial approaches) to strain the transistor. Among these approaches were high-stress capping layers and the use of embedded SiGe in the PMOS source-drain regions. Process strain creates a number of new variation challenges, both random and systematic. Researchers are beginning to focus both theoretically and experimentally on quantifying the magnitude of strain-induced variation. In [20] the authors develop an analytical model to predict threshold variation as a function of Ge fraction, layer thickness, channel length, and doping profile. This model was verified with simulations and experimental data for n- and p-MOSFETs in both single and dual-channel architectures.

Implant and Anneal

During implant and anneal process not only random dopant fluctuation can be caused, but there are other variation sources that can be created. Implant tool conditions are a significant source of transistor variation. Al-Bayati et al. [21] have studied the device sensitivity of ultra-shallow junction processes to tool-related implant and annealing parameters. In their work, NMOS and PMOS devices were studied to quantify variation as a function of the accuracy of dose, purity of dose, spike anneal peak temperature, and the ramp-up and cool-down rates. An additional variation mechanism related to implant technology arises from the poly-crystalline nature of conventional gates. Enhanced diffusion, variations in dopant activation, and implant channeling along grain boundaries can all cause increased variation. Fukutome et al. [22] have investigated the effect of randomly oriented and rotated poly-Si gate grains on lateral carrier profiles of extension regions in sub-50nm MOSFETs by direct observations and electrical measurements. By optimizing the grain boundary they were able to demonstrate a reduction in threshold voltage variation.

We have seen variation sources that can cause systematic and random variations. All these variations can cause so wide distribution of transistor threshold voltage V_{th} that cannot be correct during the design. Fig. 1.7 [9] illustrates the random variation of the

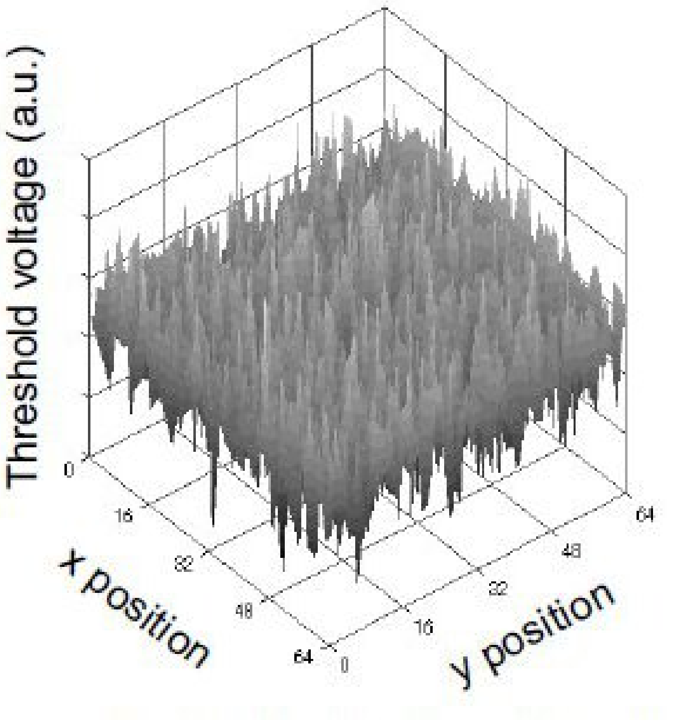

Figure 1.7: Random V$_{th}$ Fluctuation on 4k transistor [9]
Random threshold voltage fluctuation measure on closely located indetically designed 4k transistor

threshold voltage on 4k identically designed transitor and the absence of correlation suggest the presence of random perturbation as the ones depicted above.

The classical approach to characterize random perturbation, also called Variability analysis, is through multiple characterizations of statistically different device samples. The Monte Carlo method is well suited for this purpose [23] [24], but dispite the great accurancy it is quite time consuming and require large computational resources. A more efficient method is the so called *Impedence Field Method* (IFM) [25] [26] that allows to calculate the variation on the device terminal due to local parameters fluctuation through Green's function calculation. This is a linearised technique, so only variations which induce small fluctuation can be evaluated correctly with this method. The computational cost is that of small-signal analysis so it is possible to avoid repeated simulations and earn time for result analysis.

1.3 Sensitivity

As discussed at the beginning of the chapter, the request of higher performances with high reliability has enhanced the device technological progress. In the above section we have discussed of variability problem caused by small differences in the device characteristics. Now we want to discuss about the sensitivity of the device to some parameters. Sensitivity analysis is a powerful tool, especially in the optimization process, which aims at calculating the derivative of some electrical parameters, like drain current, threshold voltage etc., as a function of some internal physical or technological parameter, like dopant concentration, oxide thickness etc. .

Consider for example the shape optimization of a novel device structure. The designer must consider many different material properties, among other parameters, with respect to their dimensions and performances. In order to do this, the designer must proceed by successive steps. The first step is to identify the major dimensioning configuration, design variables and constraints on a reference design. The next step is to improve the performances or relax key constraints of the reference design by tuning physically significant design parameters. At this second level, mathematical programming techniques can be used to analyse the sensitivity of the basic design to local changes of the parameters and improve the first draft within the identified constraints.

Sensitivity analysis can be used in many different fields and can be done through different mathematical framework. In chapter 4 we will show the geometrical optimization of a Field Plate MESFET analysing its geometrical sensitivity with a Green's Function approach.

1.4 Green's function method

This thesis aims at applying the Green's function method described in [26] [27] to the variability and sensitivity analysis. In [26] the Green's function approach is used to numerically simulate the noise behavior of bipolar solid-state electron devices through a physics-based multidimensional device model. Here we want to describe how this method can be applied with succes for variability analysis and thus we present its application on the charcterization of random dopant fluctuations and random telegraph noise. Although we present the method only for two sources it can be applied on all the variability sources described above, so far as the effect are small enough to be linearized.

We will also present the use of the Green's function to the sensitivity analysis. Despite their different purposes, small-change parametric sensitivity and variability analysis of semiconductor devices have a common background: both analyses require obtaining the small-signal response of the device to an equivalent distributed charge impressed either into the volume of the device or into its surface.

1.5 Outline

This work is divided in four parts.

Chapter 2 gives a general introduction to the Drift-Diffusion model which is at the base of our analysis and presents the Impedence Field Method used to characterize MOS variability and to evaluate geometrical sensitivity. This chapter is completed with appendix A which discusses mesh problems and presents my work on a meshgenerator.

Chapter 3 gives a general presentation on random fluctuations in MOS. A completed analysis of Random Doping Fluctuations and Random Telegraph Noise on MOS devices is presented with the use of the Impedence Field Method.

Chapter 4 presents the evaluation of the geometrical sensitivity on a Field Plate MESFET with a Green's function approach. Theory and formulation of the Green's function approach to study geometrical sensitivity is presented. Validation and results are analyzed at the end of the chapter.

Chapter 5 is devoted to a general conclusion on the presented results and on further possibility of this work.

Chapter 2

Green’s function approach to variability

In the previous chapter we have discussed about variability and sensitivity analysis. In this chapter we will present a novel method which allows to characterize variability and evaluate the device sensitivity.

The study of random fluctuation can be done through experiments [30] or simulations. In simulations the most common technique is the Monte Carlo analysis where all process parameters can be varied individually or simultaneously in a more realistic approach. Despite its great accuracy, this method is time consuming and need large computational resources.

A non conventional approach is the use of the *Impedence Field Method* (IFM) [25] to treat the variations of physical parameters inside the device like linear perturbation of the system. IFM is a method based on the Green’s function technique thus is suited to evaluate the response of a linear system at a distributed source. Computing the Green’s function of the system allows to study fluctuations at the terminals due to local perturbation of the parameters inside the device.

In the following we will describe the Green’s function approach applied to the Drift-Diffusion model used in our simulations to characterize random variations.

2.1 The Impedence Field Method

The *Impedence Field Method* (IFM) was first proposed by Shockley [25] and then extended to include the noise analysis of any multiport device. IFM is a fast alternative to modeling fluctuations since only a single device needs to be simulated. Rather than solving the full nonlinear Poisson and drift diffusion equations completely for a large number of random device realizations, we obtain the solution only once, using the reference device parameters. The IFM is based on the Green's function which allows to evaluate the effect of perturbations caused by internal physical parameters fluctuations at the device terminal, e.g. we can evaluate directly the variations caused by random doping fluctuations on the drain current or the threshold voltage. The Green's function does not depend on the variation source, but is computed from the full solution of the reference device, therefore must be computed only once. The IFM has long been known from noise analysis, thus using the IFM for variability or sensitivity analysis is a noiselike approach.

We want to use IFM not for evaluating noise, but to perform a statistical sampling using a large number of realizations to characterise the device variability. The basic idea of this approach, which can be called sIFM [28] , is to evaluate the Green's function once on the reference device and to use it within a convolution integral on a large number of realizations of a perturbed device. Moreover, the effect of different variability sources can be summed if they are uncorrelated and this is the case for RDF and RTN.

The sIFM method is much faster than atomistic methods. For atomistic method, the total simulation time is directly proportional to the number of realizations of device structures in the statistical sample. For sIFM, the main computation time is spent in computing the solution for the reference device as well as the Green's function. The contribution of one additional convolution integral computation to include an additional randomization, on the other hand, is quite negligible.

2.2 Formulation

2.2.1 Drift-Diffusion model

It is well known that device can be treated at the microscopic level by Boltzmann equation, whose unknown is the distribution function of carriers, can be solved with the Monte Carlo method or with PDE models. Partial differential equations involving the central moments can be derived from Boltzmann and Poisson equations leading to a set of simplified physical models. The first three central moments can be related to the carrier concentration, the carrier average momentum and the carrier energy. This system involves the continuity equation of charge, momentum and energy which are also connected to the heat-flow of the carrier distribution. Although this system can be exploited to derive PDE systems , the computational complexity makes the approach hardly advantageous with respect to the full Monte Carlo method when the number of moments involved is higher than three.

The full Hydrodynamic model is the higher order with some computational advantages over the Monte Carlo method. It involves carrier, momentum and energy conservation together with the Poisson equation. This model can be still simplified in order to obtain models with less computational problems. Considering the average momentum dynamics fast and the average energy dynamics slow, leads to turning the momentum equation in a energy dependent relationship for the carrier velocity, thus this model is called Energy Balance. Mobility and diffusivity are energy dependent and the carrier temperature is different from the lattice temperature. A final simplification step is to neglect time dependent and space dependent variations in energy transport equation, thus relating the average carrier energy to the local electric field. Carrier mobility and diffusivity become functions of the local and instantaneous electric field. According to this model the electron and hole transport current densities are expressed as the sum of a drift and diffusion term, which together with Poisson and continuity equations make the so called Drift Diffusion model.

$$\nabla^2\phi = -\frac{q}{\varepsilon}(p - n + N^+) \tag{2.1a}$$

$$\frac{\partial n}{\partial t} = \frac{1}{q}\nabla J_n - U_n \tag{2.1b}$$

$$\frac{\partial p}{\partial t} = \frac{1}{q}\nabla J_p - U_p \tag{2.1c}$$

$$J_n = qn\mu_n\nabla\phi + qD_n\nabla n \tag{2.1d}$$

$$J_p = qn\mu_p\nabla\phi + qD_p\nabla p \tag{2.1e}$$

where ϕ is the potential, q is the elctron charge, ε si the dielectric constant, p and n are, respectively, the hole and electron concetration density, N^+ is the ionized doping concentration, J_n and J_p are respectively the electron and hole current density, U_n and U_p are the net recombination rates for electrons and holes, μ_n and μ_p are respectively the electron and hole mobility and D_n and D_p are respectively the electron and hole diffusivity.

Equations 2.1a, 2.1b and 2.1c are respectively the Poisson equation, electron and hole current continuity equations. Equations 2.1d and 2.1e are the electron and hole transport current densities equations where μ is the mobility and D is the diffusivity for electrons and holes.

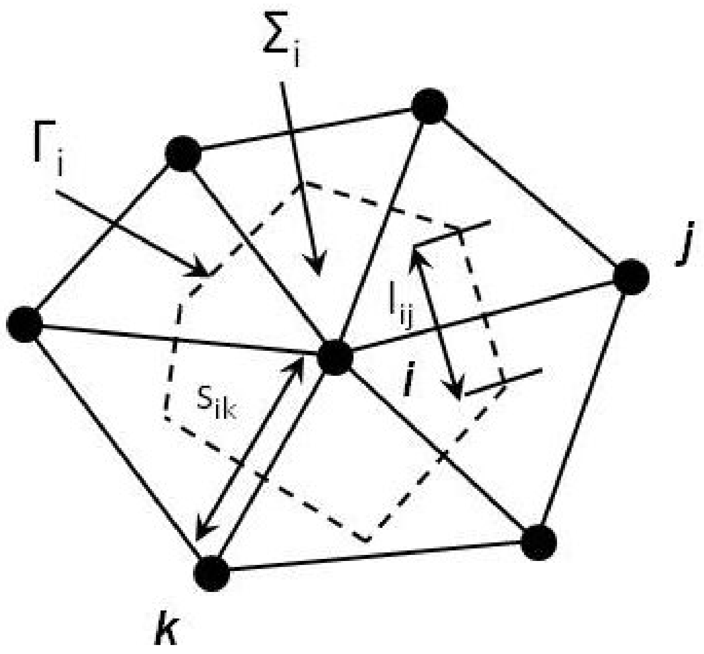

Figure 2.1: Discretization scheme
Discretization scheme where: Σ_i is the Voronoi area, l_{ij} is the length of the box side lying between node i and node j, s_{ik} is the distance between node i and node k, and Γ_i is the boundary of Σ_i

2.2.2 Finite element Box Discretization

Partial differential equations are approximated through spatial discretization by a discrete system of ordinary differential equations for numerical simulation. The most popular spatial discretization, in device simulation and not only, is the Scharfetter-Gummel finite box.

For simplicity, consider a two dimensional domain Ω discretized through a proper triangular grid, see a schematic reppresentation in Fig. 2.1. where Σ_i is the Voronoi area, l_{ij} is the length of the box side lying between node i and node j, and Γ_i is the boundary of Σ_i and n its external normal versor. Applying the Gauss theorem and approximating through a first order approach, one obtain for a scalar f and a vector F:

$$\int_{\Sigma} f \approx f_i \Sigma_i \tag{2.2}$$

$$\int_{\Gamma} F \cdot \hat{n} d\gamma \approx \sum_j l_{ij} \langle F \cdot \hat{n} \rangle_{ij} \tag{2.3}$$

The finite-boxes discretization can be directly applied to Poisson's equation assuming that the permittivity is constant, which reads, in divergence form:

$$\nabla \varphi = \frac{q}{\varepsilon} \left(\sum_k C_{Dk}^{+} + p - n \right) \tag{2.4}$$

where C_{Dk}^{+} is the net equivalent ionized donor concentration. Assuming that the potential is linear between two adjacent nodes, the resulting discretized Poisson equation is:

$$\sum_j l_{ij} \frac{\varphi_i - \varphi_j}{s_{ij}} = \frac{q}{\varepsilon} \left(\sum_k C_{Dki}^{+} + p_i - n_i \right) \Sigma_i \tag{2.5}$$

where s_{ij} is the distance between node i and j.
Now, consider electron continuity equation, the same can be done for the hole continuity equation.

$$\frac{\partial n}{\partial t} = \frac{1}{q} \nabla J_n - U_n \tag{2.6}$$

the discretization described above yields to

$$\frac{\partial n_i}{\partial t} \Sigma_i = \frac{1}{q} \sum_j l_{ij} \langle J_n \cdot \hat{n} \rangle - U_{ni} \Sigma_i \tag{2.7}$$

Side averaging $\langle J_n n \rangle$ can be carried out by taking into account that, according to the drift-diffusion model:

$$J_n \cdot \hat{n} = (-qn\mu_n \nabla \phi + qD_n \nabla n) \cdot \hat{n} \tag{2.8}$$

Assuming that the current density is constant between neighboring nodes, which means assuming that J_n is constant between node i and j, and defining a reference frame u running from node i to node j, current equation can be written as an ordinary differential equation:

$$(J_n \cdot \hat{n})_{ij} = -qn\mu_n \frac{d\phi}{du} + qD_n \frac{dn}{du} \approx -qn\mu_n \frac{\varphi_i - \varphi_j}{s_{ij}} + qD_n \frac{dn}{du} \tag{2.9}$$

The equation can be solved applying the following boundary conditions $n = n_i$, concentration at node i, for $u = 0$ and $n = n_j$ for $u = s_{ij}$.

$$n(u) = n_i \left[1 - g\left(u, \Delta_{ij}\right) \right] + n_j g\left(u, \Delta_{ij}\right) \tag{2.10}$$

where

$$g\left(u,\Delta_{ij}\right)=\frac{1-exp(\Delta_{ij}u/s_{ij})}{1-exp(\Delta_{ij}}\qquad \Delta_{ij}=\frac{\varphi_i-\varphi_j}{v_T} \tag{2.11}$$

Except for a potential difference near v_T, the above equation is strongly non linear. Inserting the approximation 2.10 into 2.9 one obtains, since the normal component of the current density is assumed to be constant between neighboring nodes:

$$\frac{1}{q}\langle J_n\cdot\hat{n}\rangle_{ij}\approx\frac{D_n}{s_{ij}}\left[n_jB(\Delta_{ij})-n_iB(-\Delta_{ij})\right] \tag{2.12}$$

where B is the Bernoulli function

$$B(x)=\frac{x}{exp(x)-1} \tag{2.13}$$

Finally, the Scharfetter and Gummel approximation for the electron continuity equation in node i reads:

$$\frac{\partial n_i}{\partial t}\Sigma_i-\sum_j\frac{D_nl_{ij}}{s_{ij}}n_j\left[n_jB(\Delta_{ij})-n_iB(-\Delta_{ij})\right]=-U_{ni}\Sigma_i \tag{2.14}$$

The complete discretized drift-diffusion model for node i is:

$$\frac{\partial n_i}{\partial t}\Sigma_i-\sum_j\frac{D_nl_{ij}}{s_{ij}}n_j\left[n_jB(\Delta_{ij})-n_iB(-\Delta_{ij})\right]=-U_{ni}\Sigma_i \tag{2.15}$$

$$\frac{\partial p_i}{\partial t}\Sigma_i-\sum_j\frac{D_pl_{ij}}{s_{ij}}p_j\left[p_jB(\Delta_{ij})-p_iB(-\Delta_{ij})\right]=-U_{pi}\Sigma_i \tag{2.16}$$

$$\sum_j l_{ij}\frac{\varphi_i-\varphi_j}{s_{ij}}=\frac{q}{\varepsilon}\left(\sum_k C^+_{Dki}+p_i-n_i\right)\Sigma_i \tag{2.17}$$

$$\frac{\partial C^+_{Dki}}{\partial t}+\sum_{j\neq k}\left(p_{jki}-p_{kji}\right)=0,\text{ for all k} \tag{2.18}$$

where the summations on index j refer to the nodes directly connected to node i.

2.2.3 Newton Method

The Newton Method, also known as Newton-Raphson method, is an iterative method for finding approximations to the roots (or zeroes) of a real function. It can also be applied to non linear systems at the condition to known how to calculate the function and its derivative in all the domain. It is widely use to solve PDE problems like the drift-diffusion model presented above 2.15.

In order to make a general discussion on the Newton method we rewrite 2.15 in a more general implicit form

$$F(x) = 0 \tag{2.19}$$

where F is a vector mapping corresponding to the discretized model and x is a vector corresponding to the values of the indipendent variables, that in our case are ϕ, n and p. The process of non linear solving consist in finding a vector of indipendent variables x^* which is a root of $F(x)$. The computational approach is via iterative step, beginning with an initial guess to x^* call x^0 and generating a new extimate x^1, that can be written

$$x^{k+1} = H(x^k) \tag{2.20}$$

where $k = 0, 1, 2, ...$ and $H(x)$ is an iterative function that have to be chosen such that

$$\lim_{k\to\infty} x^k = x^* \qquad x^* = H(x^*) \tag{2.21}$$

The most common choice of iteration function is

$$H(x) = x - S^{-1}F(x) \qquad x^{k+1} = x^k - S^{-1}F(x^k) \tag{2.22}$$

where S is a vector operator to be chosen. In the Newton's method $S = F'(x^k)$ commonly referred to as the Jacobian. Rewriting it in a more computationally convenient form, e.g. avoiding the inversion of the Jacobian matrix, Newton's method is defined at iteration k as

$$F'(x^k)\delta x^{k+1} = -F(x^k) \qquad x^{k+1} = x^k + \delta x^{k+1} \tag{2.23}$$

Therefore, two computations are performed per iteration.
A linear system of the form $Ay = b$ is solved where

$$A = F'(x^k) \quad y = \delta x^{k+1} \quad b = -F(x^k) \tag{2.24}$$

followed by the solution step 2.23. Figure 2.2 shows a schematic reppresentation of a general algorithm using the iterative Newton method to find the solution. Having as input the geometry and the mesh with the discretized physical and geometricla quantities, the first step consist in evaluating the Jacobian with a first solution x^0 on the mesh nodes. When assembling the Jacobian one calculates the residual. If the residual is smaller than the imposed tollerance value, normally smaller than 1×10^{-10}, the solution is well approximated, else the program updates the solution following 2.23 incrementing the iteration number. If the number of iteration has not reached the maximum, the Jacobian is calculated with the latest updated solution and new residual is caluclated. The algorithm stops if convergence is reached, the residual is smaller than the tollerance, or if the number of iteration has exceed its maximum, in this case the solution is not reliable.

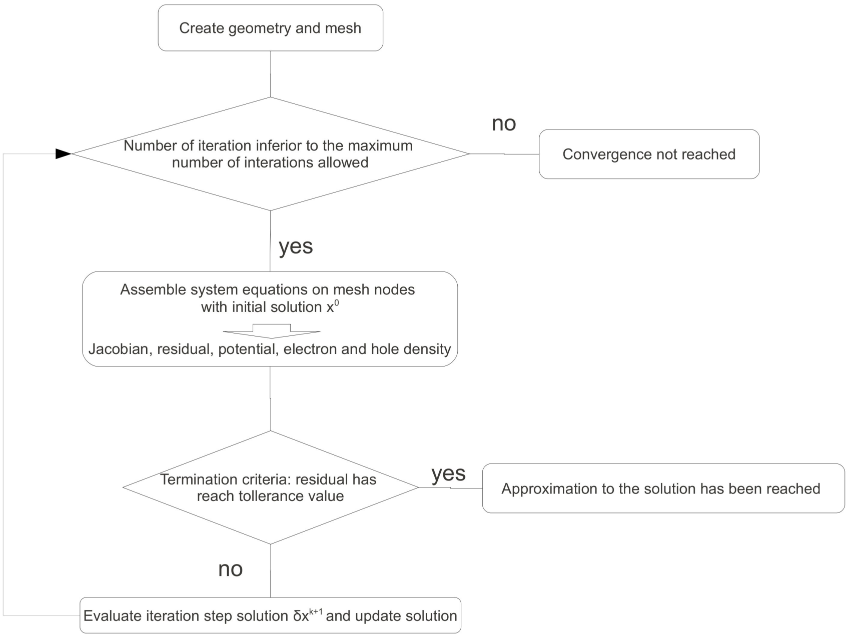

Figure 2.2: Schematic reppresentation of the solve algorithm
The scheme represent a schematic reppresentation of a general solve function which use the iterative Newton method

2.2.4 Green's formulation

The *Impedence Field Method* (IFM) was first proposed by Shockley [25] and then extended to include the noise analysis of any multiport device. It's based on the Green's function method and so it can be exploited in conjuction with every device modelling that is performed by means of the partial differential equation.

The Green's function in simple

Suppose we have to solve the system

$$Ax = b \tag{2.25}$$

where A is a differential operator and x is the array of solutions. The inverse of a differential operator is an integral operator, whose kernel is called the Green's function of the differential operator.

$$AG = \delta \tag{2.26}$$

where δ is the Dirac delta distribution.

$$x = \int Gb \tag{2.27}$$

From a physical point of view we can see the Green's function as the system response to a localized perturbation source (in this case static).

Application of the Green's function on the Drift Diffusion model

We want to apply the Green's function approach to the *drift-diffusion model* 4.17 described before. For simplicity we now express the *drift-diffusion* with the boundary conditions as the vector system

$$\mathbf{F}(\phi, n, p, \dot{n}, \dot{p}) = \mathbf{0} \tag{2.28}$$

$$\mathbf{b}(\phi, n, p, \dot{n}, \dot{p}, \mathbf{s}_e) = \mathbf{0} \tag{2.29}$$

where $\dot{x} = \dfrac{\partial x}{\partial t}$ and $\mathbf{b}$ represents the set of boundary conditions including external electrical sources $\mathbf{s}_e$.

Assuming a small perturbation, the system can be linearized around the working point. Let ϕ_0, n_0, p_0 be the working point solution and $\delta\phi, \delta n, \delta p$ the linear response to an external perturbation. Adding the microscopic noise sources s to the right-hand side of the system and adding the corresponding fluctuations to the working point, the system becomes

$$\mathbf{F}(\phi_0 + \delta\phi, n_0 + \delta n, p_0 + \delta p, \delta\dot{n}, \delta\dot{p}) = \mathbf{s} \tag{2.30}$$

$$\mathbf{b}(\phi_0 + \delta\phi, n_0 + \delta n, p_0 + \delta p, \delta\dot{n}, \delta\dot{p}, \mathbf{s}_{e0}) = \mathbf{0} \tag{2.31}$$

No other noise sources on the device boundary are taken into account, otherwise a further source term must be added at 2.31.

Perturbations must be small enough to linearly excite the device so the system can be linearized around the working point :

$$\frac{\partial F}{\partial \phi}|_0 \delta\phi + \frac{\partial F}{\partial n}|_0 \delta n + \frac{\partial F}{\partial p}|_0 \delta p + \frac{\partial F}{\partial \dot{n}}|_0 \delta\dot{n} + \frac{\partial F}{\partial \dot{p}}|_0 \delta\dot{p} = s \tag{2.32}$$

$$\frac{\partial b}{\partial \phi}|_0 \delta\phi + \frac{\partial b}{\partial n}|_0 \delta n + \frac{\partial b}{\partial p}|_0 \delta p + \frac{\partial b}{\partial \dot{n}}|_0 \delta\dot{n} + \frac{\partial b}{\partial \dot{p}}|_0 \delta\dot{p} = s \tag{2.33}$$

The system 2.32 2.33 can be solved through a Green's function approach. Let us define the Green's function $G_{\alpha,\beta}(r, r_1; t, t_1)$ $(\alpha, \beta = \phi, n, p)$ for equation α and input variable β, i.e. the response in variable α to unit source $\delta(r - r_1)\delta(t - t_1)$ injected in equation β. Like 2.27 we can calculate the fluctuations $\delta\alpha$ induced by the vector source s as the spatial and temporal convolution integrals:

$$\delta\alpha(r, t) = \sum_{\beta=\phi,n,p} \int_\Omega \int_{-\infty}^{t} G_{\alpha,\beta}(r, r_1; t, t_1) s_\beta(r1, t1) dt_1 dr_1 \tag{2.34}$$

where Ω is the system volume.

2.2.5 Advantages of the Green's function approach

To evaluate the Green's functions corresponding to the impedance field, the number of solutions required is $2N$, where N is node number, as the unit source must be added at the right-hand side of the continuity equations in each of the mesh points. The procedure is very inefficient because each time only the elements of the solution vector corresponding to the observation nodes on the contacts are relevant, while the solution on the internal nodes is discarded. From a numerical viewpoint, this procedure (also called direct method) requires one factorization of the $(3N + Nc) \cdot (3N + Nc)$, where Nc is the number contacts, of matrix equation and $3N$ back-substitutions. Taking into account the great number of grid points, it is evident that the CPU time required makes this procedure incompatible with a more efficient tools.

As opposed to the direct method, different approaches for the numerical evaluation of the Green function have been proposed in the literature, which only require the factorization of the system matrix and Nc back-substitutions. The most general approach is the so-called *Branin's Method*. This method, originally introduced for the analysis of finite dimensional algebraic linear systems [31], was applied for the first time to the physics-based noise analysis in [26]. The Branin's method can be applied to the discretized systems of equations arising either from the drift diffusion model or any other higher-order model and is well-suited for implementation in any multidimensional device simulator. Under this respect, it provides a generalization of the so-called adjoint method [32]. The latter in fact, requires the formulation of an adjoint problem with suitable adjoint boundary conditions.

The most prominent advantage of the proposed method is that the IFM is applicable to large device structures. The computational resource requirements depend only weakly on the number of randomized devices included in the statistical sample. In [28] the authors have analysed the simulation time for 3D 6T SRAM computing the sIFM for 1000 realizations of RDF. The total simulation time was of $40h$ which 50% was consumed for the DC sweep, 46% for the Green function computation and only 4% for the computation of the linear responses. It is clear that the method is more efficient as the number of realizations increase, and this is counter trend with atomistic approach.

2.3 Software Tools

In this section we will describe the tools of the Synopsis commercial simulator and the in-house developed code used to evaluate variability and sensitivity. These are the two physical device simulator software that we have used for our analysis. There are many other commercial and open-source simulator which allow to investigate physical device. In variability analysis a powerful tool named Gold Standard Simulation (GSS Ltd) was developed by the Glasgow group of Prof. Asenov. The GSS atomistic simulator, GARAND, is a statistical 3D simulator uniquely designed for the investigation of statistical variability introduced by the discreteness of charge and atomicity of matter.

The majority of device simulator based on finite element use the drift diffusion model and only a small part of them have implemented higher order models. The drift diffusion model is still valid for ultra scaled devices, but quantum correction must be taken into account.

2.3.1 Synopsis tools

Synopsis provides a set of tools to simulate electron devices starting from process to operative environment named TCAD Sentaurus.

Sentaurus Process is a complete and flexible process modeling environment. It is calibrated to a wide range of the latest technology and can be used for modern silicon and nonsilicon technologies. A process flow is simulated by issuing a sequence of commands that corresponds to the individual process steps, like annealing, implantation, etching, deposit and many others. This allow to investigate the process environment, but also to create more realistic devices.

Sentaurus Structure Editor can be used as a 2D or 3D structure editor, and as a 3D process emulator to create TCAD devices. In Sentaurus Structure Editor, structures are generated or edited interactively using the graphical user interface (GUI) or in batch mode using script, useful for parametrized device structure. It is also possible to define doping profiles and meshing strategies configuring and calling the Synopsys meshing engines. In addition, it generates the necessary input files for the meshing engines.

Mesh Generation Tools is a suite of tools that produce finite-element meshes and it is composed by three mesh generation engines:

- Sentaurus Mesh is a robust mesh generator capable of producing either axis-aligned meshes or tensor-product meshes in 2D and 3D.
- Noffset3D is an advancing front mesh generator, capable of producing triangular meshes in 2D and tetrahedral meshes in 3D. The meshes produced by Noffset3D can contain layers of elements that are nearly-parallel to given surfaces of a semiconductor device structure.
- Mesh is an axis-aligned mesh generator capable of producing meshes in 1D, 2D, and 3D.

The mesh generation is a crucial step because influences many aspect of the simulation. The computational cost and time is directly proportional to the number of nodes and the convergence to the solution is faster for a good mesh which needs less iterative steps. For example, for a 3D MOS device which present curved surfaces the best choice is of Noffset3D that creates element layers parallel to the surfaces. In 2D devices the difference between the mesh generators is not so appreciable [29].

Sentaurus Device is capable of simulating the electrical behaviour of a single semiconductor device self-standing or a few physical devices, maximum eight, combined in a

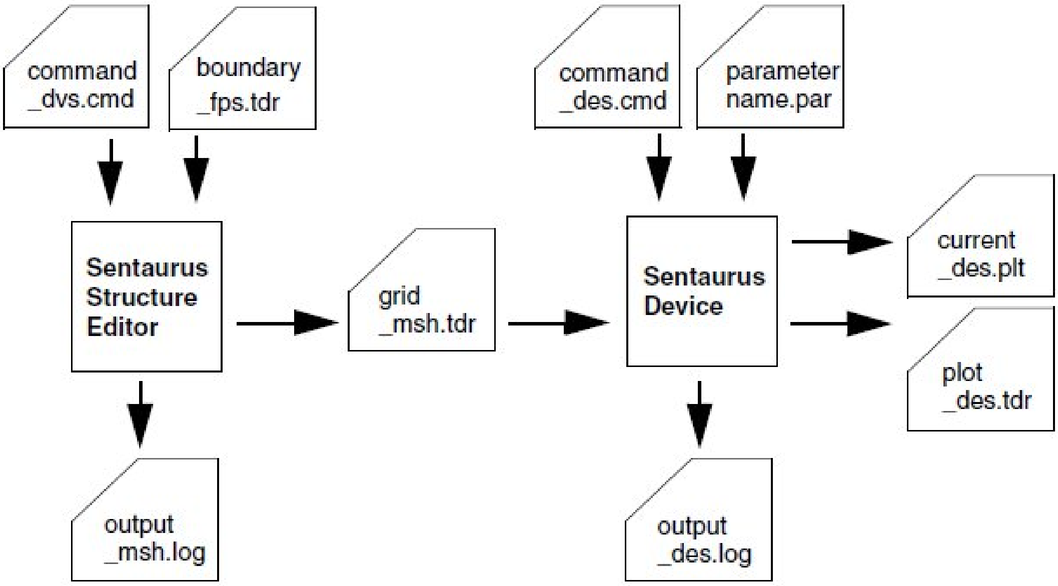

Figure 2.3: Synopsis tool flow

Typical tool flow with device simulation using Sentaurus Device. Sentaurus Structure Editor allow to create geometry and mesh process simulation if needed. The output is saved in the grid file. Sentaurus Device use the grid file to run physical simulations. Results are written in two separeted file. The *plot des.tdr* file contains internal physical paramteres, e.g. potential, electric field etc. and the *current des.plt* file contains terminal charcteristics, e.g. drain current, gate voltage etc.

circuit. Terminal currents, voltages, and charges are computed based on a set of physical device equations that describe the carrier distribution and conduction mechanisms. Sentaurus device needs at least the grid file of the structure and the command file as input, see Fig. 2.3 where a typical tool flow is represented. Extra input files can be defined to use non-standard parameters. The command file is mainly divided into three parts where to specify the physical model, the mathematical options and the operative conditions, plus other minor parts used to specify the I/O variables and formats. Refer to the Sentaurus Device manual for all the details [50].

Once parametrized the command file, simulations are run and one must handle a large amount of data files. Synopsis designed a powerful tool named Sentaurus Workbench which makes the use of Synopsys TCAD tools easier. It frees the user from typing system commands for the handling of data files or starting applications. One of its main advantages over a traditional simulation session is the possibility of parametrizing input files to run groups of simulation automatically with the corresponding data flow. Fig.

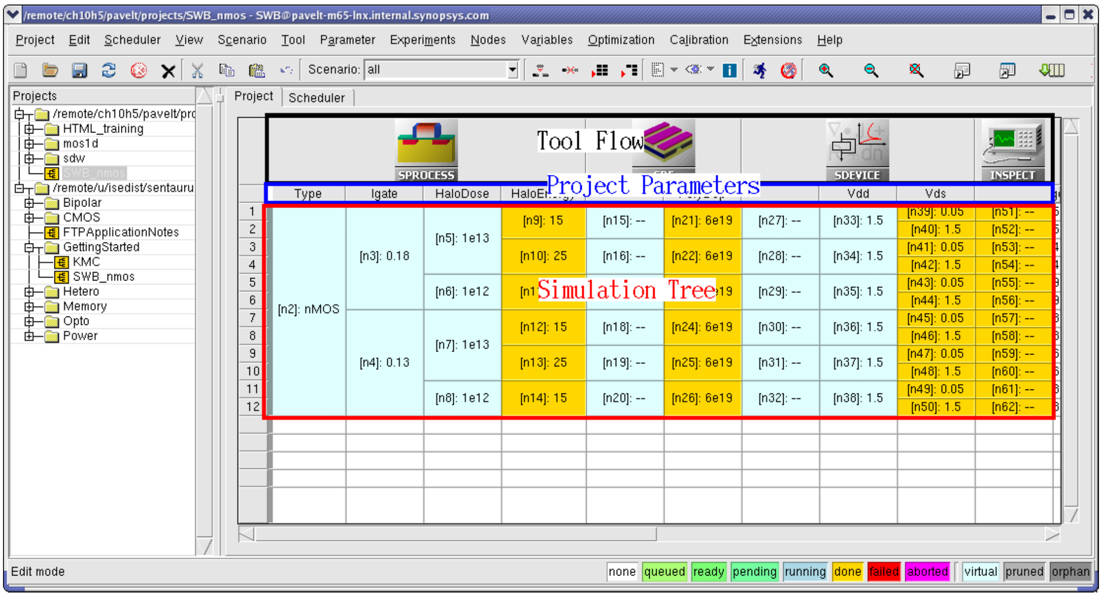

	Type	Igate	HaloDose	HaloEn				Vdd	Vds	
1	[n2]: nMOS	[n3]: 0.18	[n5]: 1e13	[n9]: 15	[n15]: --	[n21]: 6e19	[n27]: --	[n33]: 1.5	[n39]: 0.05	[n51]: --
2									[n40]: 1.5	[n52]: --
3				[n10]: 25	[n16]: --	[n22]: 6e19	[n28]: --	[n34]: 1.5	[n41]: 0.05	[n53]: --
4									[n42]: 1.5	[n54]: --
5			[n6]: 1e12	[illegible]	[illegible]	[illegible]	[n29]: --	[n35]: 1.5	[n43]: 0.05	[n55]: --
6									[n44]: 1.5	[n56]: --
7		[n4]: 0.13	[n7]: 1e13	[n12]: 15	[n18]: --	[n24]: 6e19	[n30]: --	[n36]: 1.5	[n45]: 0.05	[n57]: --
8									[n46]: 1.5	[n58]: --
9				[n13]: 25	[n19]: --	[n25]: 6e19	[n31]: --	[n37]: 1.5	[n47]: 0.05	[n59]: --
10									[n48]: 1.5	[n60]: --
11			[n8]: 1e12	[n14]: 15	[n20]: --	[n26]: 6e19	[n32]: --	[n38]: 1.5	[n49]: 0.05	[n61]: --
12									[n50]: 1.5	[n62]: --

Figure 2.4: Sentaurus Workbench screen shot

Sentaurus Workbench screen shot which allows to run sequences of simulations giving the possibility to easily handle many data.

2.4 show an example of Sentaurus Workbench tool flows.

Despite all this powerful tools it's not always easy to do what one needs. For example, I had to modify the charge on a single node, which is a very simple task to do in our in-house code, but not in the commercial software. It seems that there's no free access to all data and no more the possibility to modify certain data on the structure file. Among others, it's for this reason that many research group decide to develop their own simulator.

2.3.2 In-house simulator - POLITOFBZ

The need of researches groups to simulate novel models, or to completely manage the simulation files as described in the above section, has lead to the development of specific simulation software. The principal problem of these tools is that the main objective is only a small part of all the simulator software, e.g. the physical simulation engine, so one has to spent a lot of time in creating a user interface and algorithms to absolve task that are not of primary interest. The software structure is normally not optimized because of lack in programming techniques and so simulations are slower and with a lower reliability compared to commercial tools. Despite these reasons, scientific

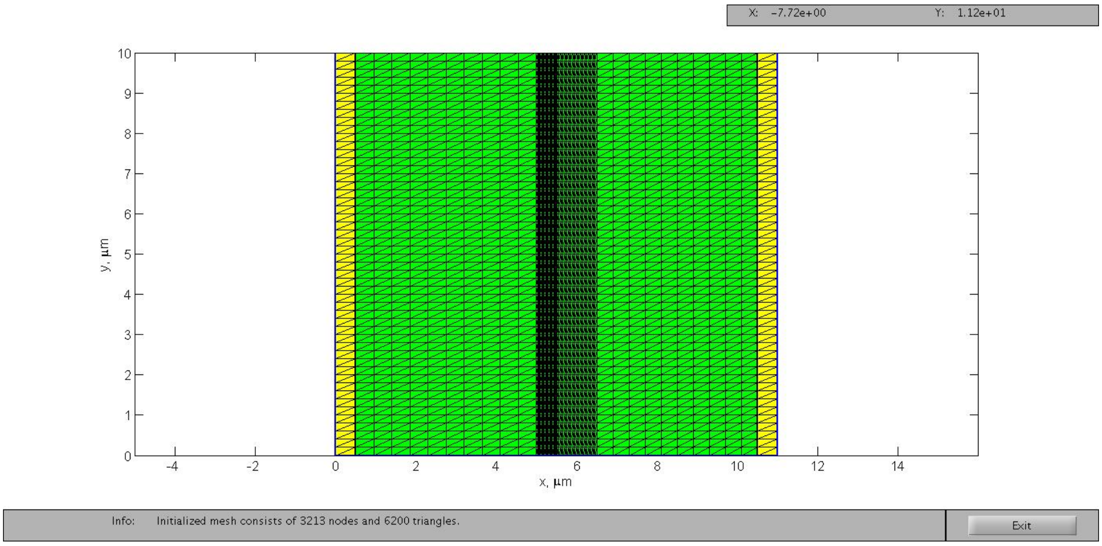

Initialized mesh consists of 3213 nodes and 6200 triangles.

Figure 2.5: FEM GUI simulator PolitoFBZ screen shot
Example of a FEM GUI screen shot of the PolitoFBZ simulator which allows to create 2D structures and the relative mesh.

programmer has created powerful tools has the one created within our simulation group. The in-house simulator implements the 2D Drift-Diffusion model, in Matlab and Fortan, with a box discretization as described in 2.2.2 to model the system. The solution of the system is evaluated through the iterative Newton method which allows to calculate an approximation of the non linear system solution only if it's possible to calculate the function and its Jacobian in all the domain.

Structure and simulations can be handled through a simple GUI 2.5 and a command file. The mesh generator is simple, but give good results. A more powerful grid generator, also adapt for 3D extension, implemented during my thesis work is presented in the appendix A.

The main characteristics of this simulation tool is the implementation of a small and large signal solver using the harmonic balance. It also implement the Green's function formulation previously described including trap rate equation, in combination with recombination and mobility models.

Chapter 3

Random Fluctuations

In the first chapter we have briefly described many sources of random variability. Now we want to characterize more in detail the effect of two of them, Random Dopant Fluctuations and Random Telegraph Noise. The first is recognized as the major source of variability in actual device technology, while the second plays a major role in memory devices.

Random fluctuations are the real challenge of further scaling because of their microscopic nature. The fluctuation in the number of dopants in the channel, of the order of three/four atoms, will not influence the 130 nm node where the dopants are a few hundreds, while the same amount of fluctuation will have a great influence in the 22 nm node where the dopants are of a few decades. Also the dopant position becomes important for a small number of dopants. The results are devices with large distribution of electrical characteristics, e.g. the threshold voltage V_{th} or the drain current Id, which cannont be controlled by design.

Random dopants fluctuations influence, more or less, nearly all devices. In memory devices a major problem, in addition to RDF, is represented by the presence of traps in the gate oxide. The presence of a single trap, and the consequent trapping and detrapping of electrons, in some position can have a great influence on the threshold voltage causing a possible error in the reading operation. Naturally, the presence of a trap in the Si-SiO$_2$ interface between channel and gate will not have a great influence on a gate length of 1 μ m, but the same trap has a great influence on gate length of 22nm. Moreover, as the device is scaled the threshold voltage is reduced, so the same amount of variation caused by trapping and detrapping of the trap, has a different influence on the actual reference value: a V_{th} shift of 50mV for a $V_{th} = 1,5$V corresponds to a variation of 3% while for a $V_{th} = 0,7$V corresponds to a variation of 7%.

In this chapter we will present a variability analysis using the statistical Impedance

Field Method on a MOS device in 2D and 3D dimensions, considering RDF and RTN together and self standing.

3.1 Simulation setup

The tested device is the MOS device represented in Fig. 3.1, subpart of a floating memory device. The structure has been created with Sentuarus Structure Editor using the process emulator. The complete command file can be found in the appendixB.
The structure represented in Fig. 3.1 present a substrate region with a uniform doping $Na = 2e18$ cm^{-3} thickness 500 nm and section 64 nm$\times$ 64 nm. The nominal MOS gate length is $Lg = 32$ nm, width $W = 32$ nm and the oxide thickness is $Tox = 0,8$ nm. This structure is a basic structure that can represent also memory , for example replacing the gate oxide with a ONO box (Oxide-Nitride-Oxide). Drain and Source are created using a Gaussian profile with a peak value of doping of $1e20$ cm^{-3} of depth 25 nm and a ratio factor of $0,5$.
The mesh is created using *Noffset3D* which is the best choice. Fig. 3.1(b) shows the generated mesh that presents a high density of nodes in the silicon region at the Si-SiO$_2$ interface. The mesh smoothly relaxes in the oxide region where we have the interest to fully characterize the electrostatic effect of trapped charge. Drain and source are also regions with a dense mesh, while it relax along the bottom of the substrate.
The 2D structure, see Fig. 3.2, has been extracted from the 3D structure with a cut at center of the channel. In this case the simulator considers the width W equal to 1 μm. The 2D MOS has been used as a first step, before the 3D simulations, to validate the presented model and have more accurate grid.
Simulations are run with Sentaurus Device, an example of a complete command file can be found in appendixB. No specials physical models have been activated except for the mobility where dependeces on electrical field and doping have been activated.

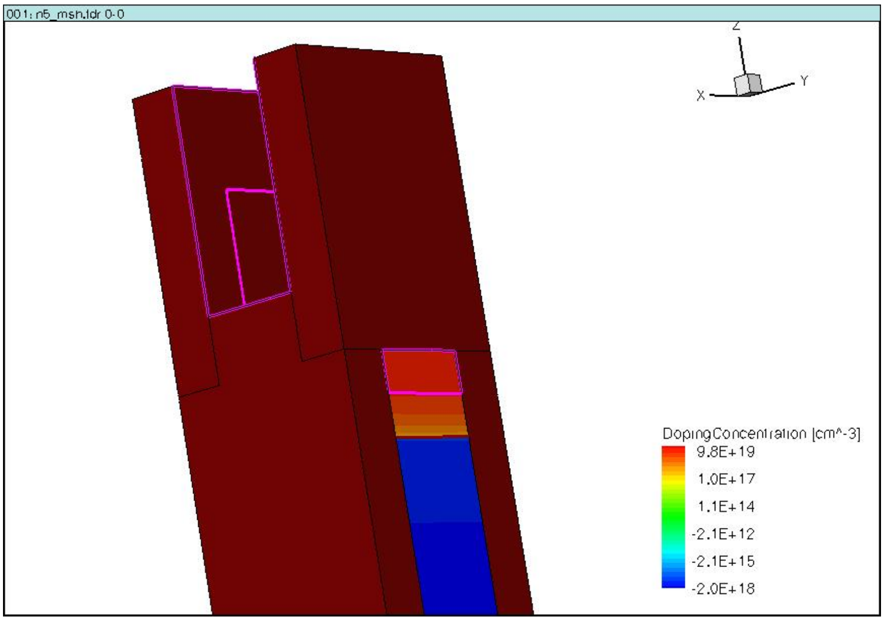

(a) MOS 3D

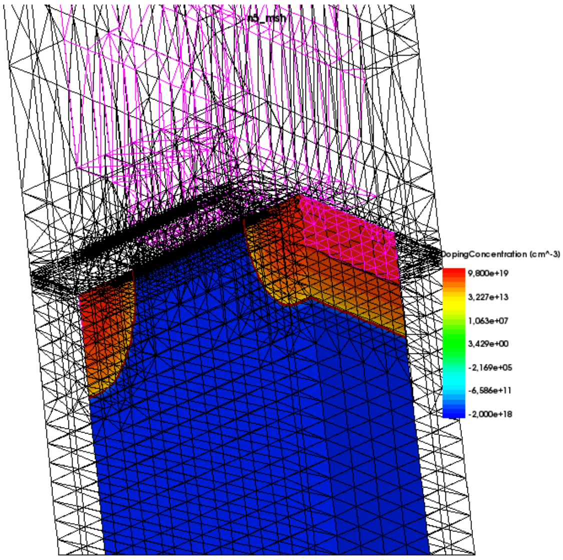

(b) MOS 3D mesh

Figure 3.1: 3D MOS device

3D MOS device zoom of the channel region. The red regions are isolation stacks of polysilicon. (a) shows the doping concentration. (b) shows the mesh where the oxide and poly silicon regions are transparent.

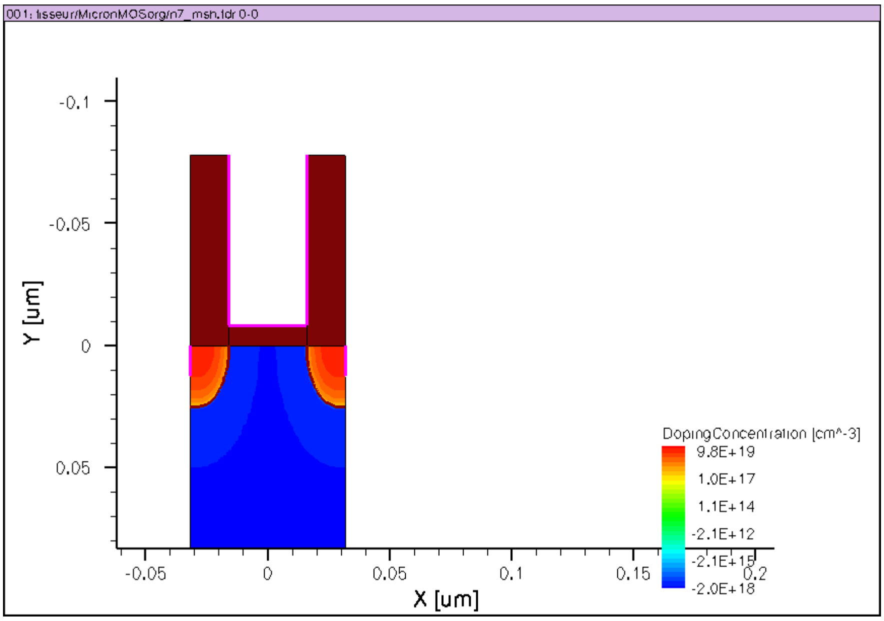

(a) MOS 2D

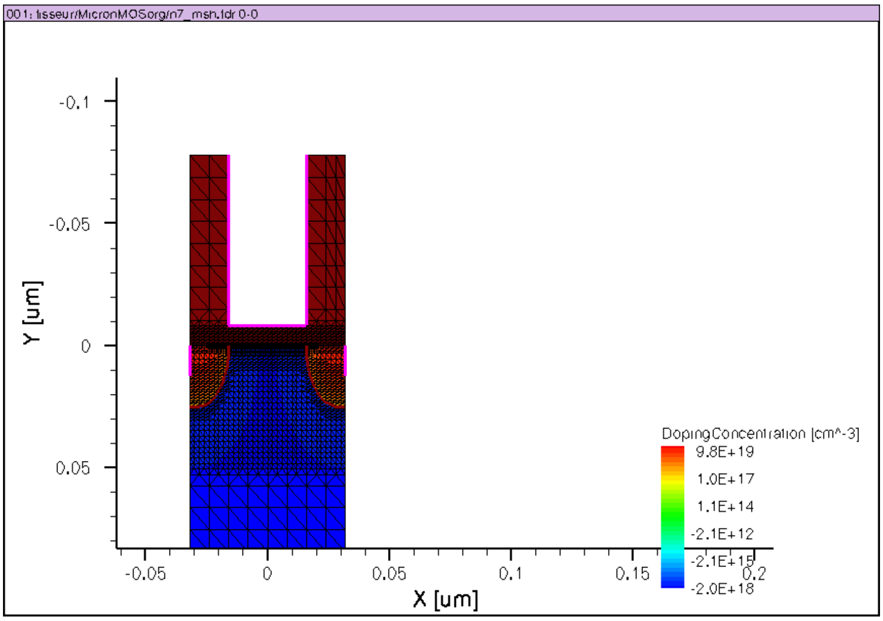

(b) MOS 2D mesh

Figure 3.2: 2D MOS device

2D MOS device zoom of the channel region. (a) shows the doping concentration. (b) shows the mesh

3.2 Random Dopant Fluctuations

The steady lowering of supply voltages, to reduce the power consumption and to hold the reliability, makes the systems based on MOS based devices more sensitive to fluctuations in the device characteristics. As the device is scaled the number of dopants is reduced, see Fig. 3.3 , and lead to a major influence of random fluctuations of the relatively small number and their placement in the channel, inducing significant variations on the threshold voltage and drive current.

Dopant atoms fluctuations issue has been pointed out in [33] [6] and a first analitically approach has been presented in [34]. RDF has been largely studied in the recent decade and is identified as one of the major sources of variability in nominally identical adjacent devices. Analytical models attempting to estimate the threshold voltage standard deviation σV_{th} are based on the variance in dopant number in the channel region of the transistors, which is known to follow a Poisson distribution. The analytical formulation, Stolk's formulation, that is recognized to better charcterize RDF has been presented in [35]

$$\sigma V_{Th} = \left(\frac{\sqrt[4]{4q^3 \varepsilon n_{Si} \phi_B}}{2} \frac{EOT}{\varepsilon_{ox}} \frac{\sqrt[4]{N}}{\sqrt{W_{eff} L_{eff}}} \right) \tag{3.1}$$

where $\phi_B = 2k_B T ln(N/n_i)$ (with k_B Boltzmann's constant, T the absolute temperature, n_i the intrinsic carrier concentration, q the elementary charge, EOT is the equivalent oxide thickness, N is the substrate doping, and ε_{Si} and ε_{ox} are the permittivity of the silicon and oxide respectively. The effective channel length L_{eff} and width W_{eff} are used instead of the physical values in order to correct for offsets in the active device area. However, equation 3.1 underestimates σV_{th}. Full scale numerical simulations have shown [36] that the dopant number fluctuation is insufficient to explain the true magnitude of the threshold voltage fluctuation. The randomness in the dopant arrangement in devices with having identical number of dopants in the depletion region contributes further to V_{th} variability due to the spatial inhomogeneities in the potential and corresponding current percolations.

However, the analytical models capture essential aspects of threshold voltage variability. It is inversely proportional to the oxide capacitance, and increases with the substrate doping. Therefore, further reduction of EOT reduces V_{th} variability, but the benefits of this scaling trend are cancelled by the faster increase in channel doping that is needed to maintain the electrostatic integrity of a planar bulk MOSFET,i.e. short channel effect SCE. In addition, the area reduction of a bulk MOSFET with scaling also contributes to increasing V_{th} variability.

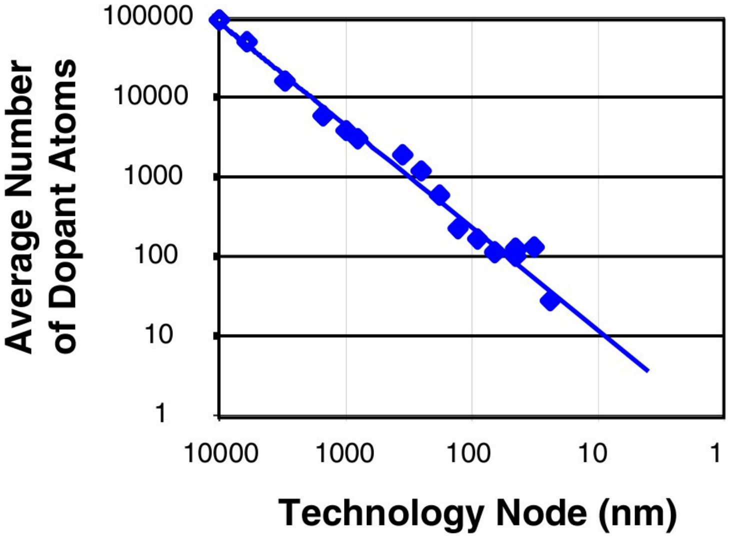

Figure 3.3: Average number of dopants atom Average number of dopants atom in the channel in function of the technology node [8]. It give a clear idea in dopant number differences.

Through simulations results it has been demonstrated in [37] that RDF is $\backsim 65\%$ of the total NMOS$\sigma_{V_{th}}$ for the 65nm node and $\backsim 60\%$ of the total PMOS$\sigma_{V_{th}}$ for the 45nm node. To properly evaluate variations between two adiacent devices, additional effect must be added to the above formula, as it has been demonstrated also in [30] suggesting that there are other important sources of fluctuations, e.g. LER and LWR.

In the atomistic method of simulating effects due to RDFs in a device, a large set of 3D devices that have microscopically different doping profiles is simulated. The key point in this kind of simulations is the method used to generate the dopant randomization. It is possible to use a Monte Carlo process simulation. Atomistic MC methods developed for the simulation of implantation and annealing steps, are widely used in TCAD simulations for the simplicity of implementation and their accuracy. However, they are not suitable for a RDF analysis where a large ensemble of devices has to be modelled. Models that do not require such a large CPU time and that avoid processing simulation steps are preferable for RDF analysis. They are used under the assumption of a uniform doping concentration and then the doping profile is randomized according to the desired method. A powerful tool for the analysis of RDF is randomize a continuum doping profile using different methods such as Sano [38], nearest grid point

(NGP) that assigns the doping of a particle to the nearest mesh node, or cloud-in-cell (CIC) where the doping of a particle is distributed to the vertex nodes of the element in which the particle is located. Such methods may in general predict the physics of RDF, but they rely on the assumptions of each type of model, and particular care has to be taken because are parameter dependent.

In [39] the dopant density varies at each mesh node in accordance with the number of dopants generated in each mesh via the Poisson distribution. This approach has been extended to the extreme atomistic regime, where most meshes contain no dopant or, at most, one dopant, in order to represent the graininess of the dopants [40]. However, it is not at all clear whether such a naive extension of the conventional dopant model expressed by continuous to the atomistic where all dopants inside the entire device regions are treated as being discrete, is consistent with the physics presumed in the DD simulation scheme.

In [38] Sano proposed a method which relies on the assumption that the dopant atoms produce long and short range Coulomb interactions that give rise to screening between each dopant. The characteristic length scale that separates the range of these interactions is given by the mean separation of dopants lc , called screening length:

$$lc \approx \frac{1}{2} N_a^{-1/3} \tag{3.2}$$

where Na is substrate doping.

The inverse of the screening length is the screening factor kc which is a cut-off parameter, that is

$$kc \approx 2 N_{ac}^{1/3} \tag{3.3}$$

It is obvious that this model strongly relies on the choice of the screening length, due to the fact that eqs. 3.2 and 3.3 represent magnitude orders estimations. The dependence on the screening length is evident from the fact that if lc is too small compared to the average meshing step size, then screened charges are highly localized in the regions where each dopant atom resides. In this case the dominant part of the interaction is represented by the short-range screened potential. On the other hand, if lc is too high, screening effects are averaged out and the doping profile appears smooth, and the decaying long-range potential represents the dominating part of the interaction. In the first limit $lc \longrightarrow 0$ the dopant density resembles a δ-function, whose peaks reside in the position of each atom. In the opposite limit $lc \longrightarrow \infty$ the doping profile resembles a continuous and uniform doping concentration.

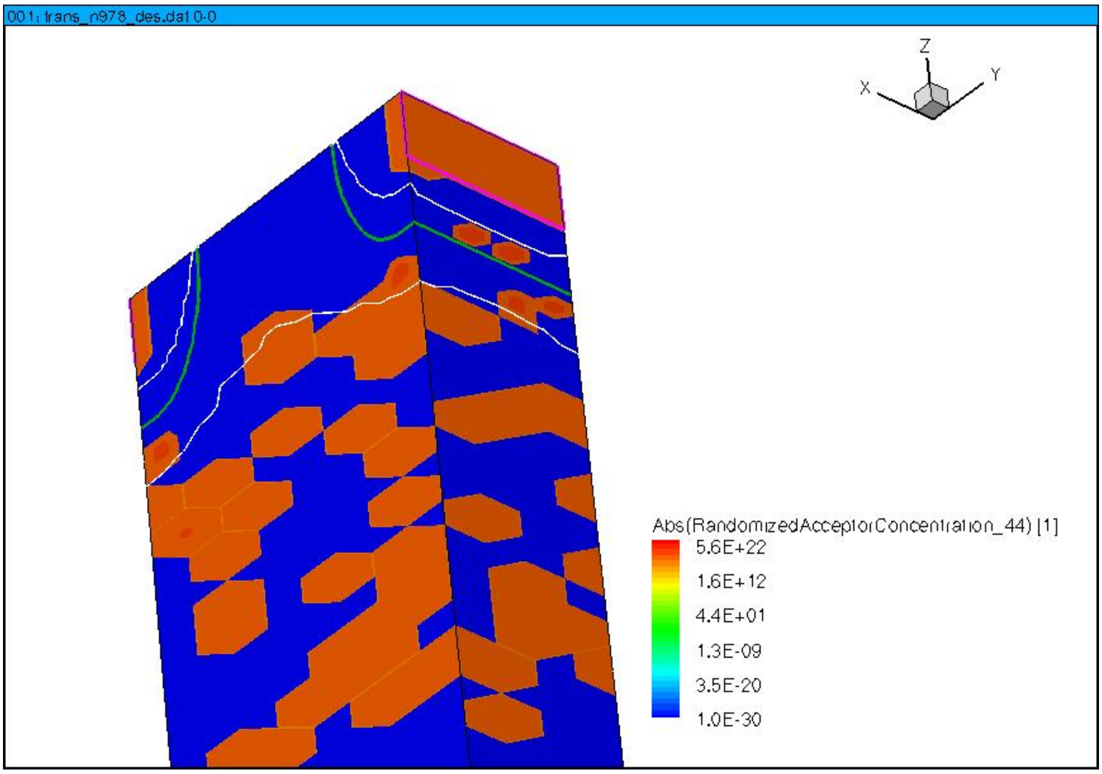

Figure 3.4: Example of RDF realization
Sentaurus device can create a large number of random realization as the one represented in the figure.

3.2.1 Green's function approach to RDF

To analyse RDF we propose the impedance field method which represent a fast alternative to modeling RDFs since a single simulation is sufficient. In the IFM, the local doping fluctuations are assumed to be small enough to alow the equation system to be linearized around working point condition. The IFM can be used to compute the fluctuations of the terminal characteristics as a result of RDFs and also allows to identify the location of the dominant fluctuations contributions within a semiconductor device and, therefore, in principle to design RDF-resistant devices.

To characterize random dopant fluctuations we have used the Impedence Field Method implemented in Synopsis [50] . This method generates a large number of randomized doping profiles from the average doping profiles present in the grid file of the simulated device, see Fig. 3.4. Acceptor and donor concentrations are randomized independently, assuming dopants are spatially uncorrelated and using a Poisson distribution function.

So the probability to find exactly k dopants in the box for vertex i is:

$$P_i(k) = \frac{(N_i V_i)^k}{k!} exp(-N_i V_i) \tag{3.4}$$

where i is the index of the vertex with volume V_i and an average doping concentration N_i. This method must be specified in command file of Sentaurus Device defining the number of random samples and the seed for the random number generator.
For costant voltage at contact c, the fluctuation of the current at contact c due to RDF, fluctuation in the doping profile $N_v(r) - N_{ref}$ is linear and can be evaluated through the following equation as generally presented in chapter 2.2.4 :

$$\delta I_c = \int_{\Omega} d^3 r G_{Ic}(r)[N_v(r) - N_{ref}(r)] \tag{3.5}$$

where Ω is the device volume, G_{Ic} is the Green's function of c contact current, N_{ref} is the reference doping distribution and N_v is each of the random doping realizations. The Green's function depends on whether the change in current or voltage is being computed, the bias conditions, and the transport equations. It also depends on the device structure, mesh,models and their parameters. However, the Green's function is independent of specific random doping profiles. Due to linearization, only one full device simulation is required to obtain the Green's function, from which the change of terminal characteristics for any given doping variation can be computed easily.
This model has been validated by Synopsis in the application note [41] and it has began to be used by other authors [42].

3.3 Random Telegraph Noise

Random Telegraph Noise (RTN) is known since the days of vacuum electronics and it was also called burst or popcorn noise when observed on bipolar devices. RTN has become an important challenge in submicron technologies. Indeed, with aggressive CMOS scaling and increased parameter variability, RTN has emerged as a critical limiting factor producing transient failures in SRAMs, DRAMs, oscillators, PLLs, and many radio frequency (RF) circuits. The first observation of RTN in MOSFETs has been reported in 1984 [43]. An RT signal consists of the random switching of the current through a device between a high and a low state. In this two-level case, the RTN is characterized by three parameters: the up time τ_{up}, the down time τ_{down} and the amplitude δI_d. While the up and down times are randomly distributed, the amplitude is usually fixed and can be determined through experiment. When analysing the RTN for

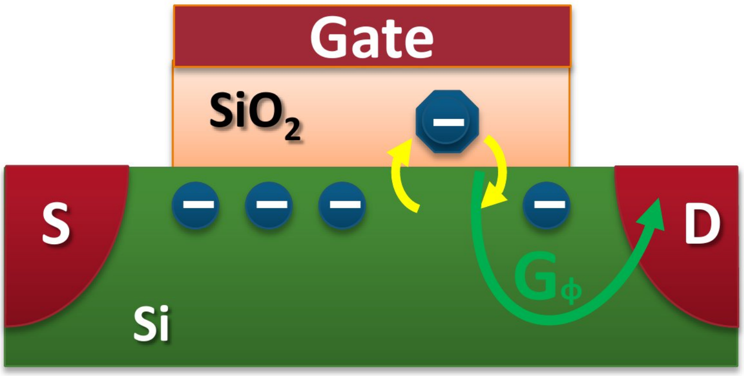

Figure 3.5: RTN schematic representation
The presence of a trapped charge in the gate oxide can be evaluated through the Green's function.

a sufficiently long period of time, one can establish the probability distribution function of the switching times, which appear to be Poisson distributed [44], and, hence, can be described by:

$$P_1(t) = \frac{1}{\tau_1} exp(-t/\tau_1) \tag{3.6}$$

with τ_1 the average time constant and $P_1(t)dt$ the probability that the high state 1 will not make a transition for time t, then will make one in the interval t and $t + dt$. The average time constant depends generally on the operating conditions of the MOS transistor and based on this dependence, one can identify the average up and down time constants with the capture τ_c and the emission τ_e time constants of the responsible trap, which usually resides in the gate oxide or at the interface. RTN can be also seen as a useful tool to study oxide traps, revealing information on their energy level, capture cross section and even depth and lateral location [45].

While invaluable information on trap behavior in gate dielectrics has been gathered over the years by lengthy, time-consuming RTN studies on single transistors [43] [44] [45] [46], it has become clear that in order to quantify its possible impact on the circuit level, a statistical approach is required, whereby a large set of devices is measured in a reasonable time. This is mainly related to the fact that RTN amplitude exhibits a wide range of values. This has been explained by considering the non-uniform potential landscape at the Si/SiO2 interface induced by the random distribution of fixed oxide charge in the gate dielectric and by the random dopant fluctuations in the substrate [51]. This leads to current filamentation in weak inversion and anomalously large RTNs when the trap is located in a strategic position controlling a percolation path [47].

Nowdays, Random Telegraph Noise is attracting the attention of the nonvalatile memory community and becomes one of the main issues to be considered in the development of future floating-gate and charge-trap technologies. The severe scaling process of nonvolatile memory boosts the attention on RTN which has a great influence in V_{th} stability. In fact the presence of spurious charge trapped in the tunnel oxide (being process-induced or resulting from cell operation) influences, in a non negligible way, both the program/erase (P/E) transients and the trapping/detrapping dynamics after P/E, i.e., when a nonstationary trap-filling condition exists. Second, and more remarkable, even when the tunnel oxide traps have reached their equilibrium condition, the threshold voltage V_{th} may result unacceptably unstable. The magnitude of RTN grows as 1/WL, a rate much faster than many other sources of variability [49]. In the future, therefore, it is expected that RTN will affect more adversely.
Random variations of cell V_{th} may in principle give rise to erroneous data reads or erroneous program operations in non-volatile memories, since programming algorithms include verification steps which can fail in presence of large V_{th} fluctuations.

Green's function approach to RTN

Here, we want to present a novel approach to study RTN using the Green's function method described in chapter 2.2.4. We consider the presence of a single trap in the Gate oxide region which can be full or empty, neglecting trapping and detrapping dynamics. The presence of a trapped charge in the oxide influence the right hand side of the Poisson equation. So the Green's function that we have to calculate is the one relative to the Poisson equation at the trap position. What we want to characterize is the influence of RTN on the threshold voltage shift V_{th}. To do this we evaluate the drain current shift with the relative Green's function of the Poisson equation $G_{D,\phi}$ and the convolution integral formula described in chapter 2. In this case, the local perturbation of the trapped charge is a Dirac delta $\delta(x_{trap})$ localized at the trap position, so the convolution integral is reduced to a simple product

$$\Delta I_{D,IFM} = q_{trap} * G_{D,\phi}(x_{trap}) \tag{3.7}$$

where q_{trap} is the trapped charge, usually one electron, and $G_{D,\phi}(x_{trap})$ is the green function evaluated at the working point that correspond to the nominal threshold working point condition. Once we have the drain current shift $\Delta I_{D,IFM}$ we use the Y_{dg} parameter extracted by a small-signal analysis to evaluate the voltage shift at the Gate.
The method is vary simple and fast. Summarinzing, the first step is to calculate the Green's function of the Poisson equation relative to the drain current on the refercence

device with no traps at the working point of interest, e.g. at the threshold voltage. The second step is to use the value of the calculated Green's function at the position where we want to place the trapped charge and multipling it with the trapped charge value, obtaining the drain current shift. The final step consist in using the Y_{dg} calculated by the small signal analysis to translate the drain current shift in the threshold shift.

3.3.1 Green's function validation

The Green's function approach to RTN described in 3.3 has been validate on the MOS structure described in 3.1. The Green's function $G_{D,\phi}$ has been calculated and extracted from Sentaurus device simulations results.

First we have validated the Green's function approach in 2D simulations, comparing our approach with direct simulations of the trap effect for different positions, named incremental approach. The incremental approach consist in directly evaluating the trap effect running simulation adding the effect of a trap in varying positions and calculating the drain current $I_{D,trap}$.

Sentaurus Device provides several trap types (electron and hole traps, fixed charges), different types of energetic distribution, and various models for capture and emission rates. Traps are available for both bulk and interfaces. Fixed Charge traps are the type of traps that are always occupied. This last it's not our goal.In addition to the fixed charge we have used the *single trap* option which is used to mimic the behavior of a single fixed-charge trap selecting between negative or positive charge type. Naturally, when defining the trap characteristics is possible to choice every positions in the device, also at the interfaces, and the fixed charge is set on the nearest mesh node.

The drain current shift is thus calculated differentiating the reference drain current with the ones calculated with the filled trap $\Delta I_D = I_{D,empty} - I_{D,trap}$. The trap positions has been varied from source to drain and at three different distances from the interface: the first row of mesh nodes under the Si-SiO$_2$ interface in the channel region fig. 3.7, on the Si-SiO$_2$ interface fig. 3.6, and at the first row of mesh nodes over the Si-SiO$_2$ interface in the oxide region fig. 3.8. These positions represent the most potentially critical ones. The comparison has been made at different working point conditions, at $V_{GS} = 0,86$ V and $V_{DS} = 0,1$ V that is at threshold condition, at $V_{GS} = 5$ V and $V_{DS} = 0,1$ V and at $V_{GS} = 0,86$ V and $V_{DS} = 2.5$ V. The three figures 3.7, 3.6 and 3.8 show an excellent agreement between the Green's function approach (blu line) and the direct evaluation of the trap effect (red symbols) in all the tested conditions. The agreement between the two approach demonstrates that RTN induces fluctuations that can be linearised, thus it

is possible to use the Green's function approach.
From the figures it is also possible to analyse the dependence of the trap positions along the channel on the drain current. Near threshold conditions $V_{GS} = 0,86$ V and $V_{DS} = 0,1$ V the traps in the middle of the channel have a stronger effect then the ones positioned a the sides of the channel. For high gate voltage $V_{GS} = 5$ V the average effect is reduced.

We have also tested our approach on the 3D MOS structure, but meeting some problems. The Green's function approach eq. 3.7 is not coherent with the incremental of the trap effect. The error is of nearly the 50%, but we haven't understood if it is a problem of the implementetion or if it is due to the fact the RTN effect can not be linearised. In the 2D simulations the device extends for 1 μm in the width direction while in the 3D the width is 32 nm. We have also tried to work around the problem inserting a small amount of charge on the single node to test the Green's function alone as a function of the grid, but the simulation software doesn't allow to control the amount of node trap charge.

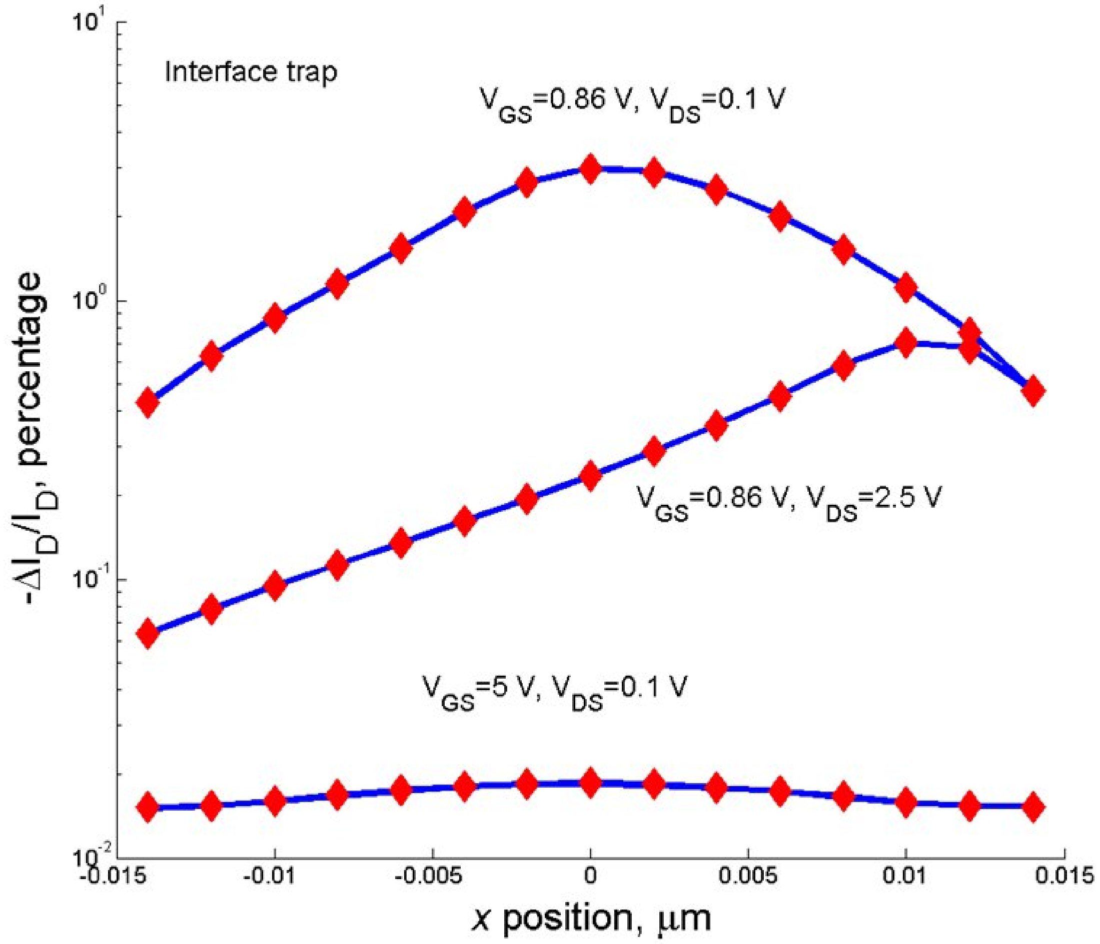

Figure 3.6: Comparison between incremental and Green's function. Si-SiO$_2$ interface. Comparison between the incremental (symbols) and Green's function (line) estimation of (minus) the relative drain current variation $\Delta I_d/I_d$. Trap placed at the interface between Si-SiO$_2$.

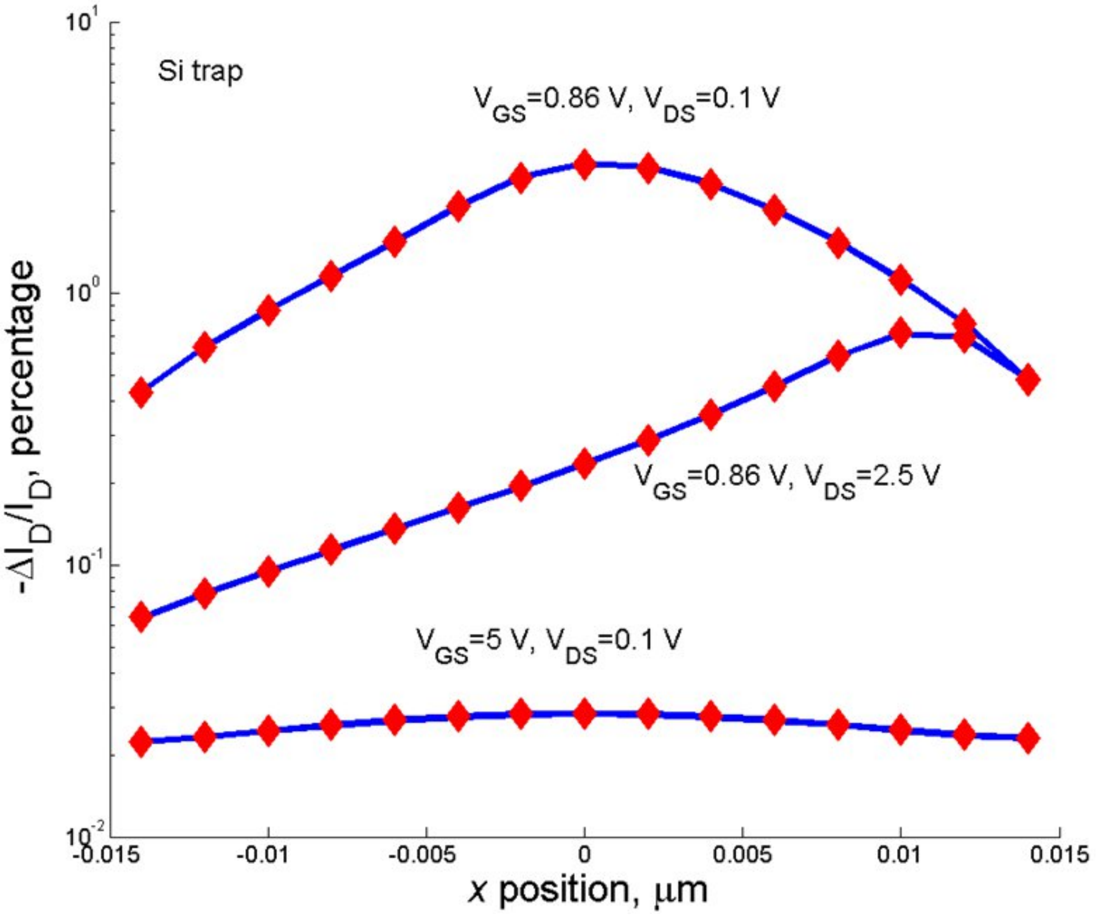

Figure 3.7: Comparison between incremental and Green's function. Traps in the Si region. Comparison between the incremental (symbols) and Green's function (line) estimation of (minus) the relative drain current variation $\Delta I_d/I_d$. Trap placed in the Si region.

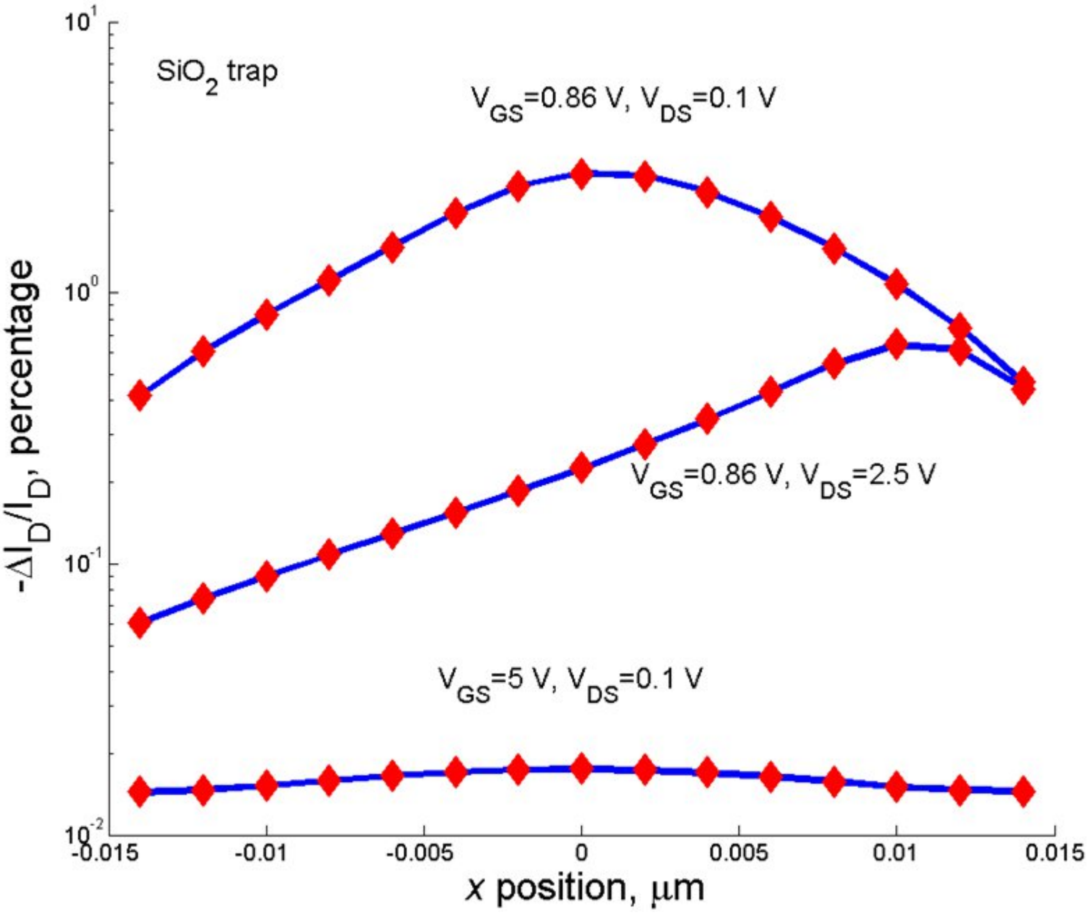

Figure 3.8: Comparison between incremental and Green's function. Traps in the SiO$_2$ region. Comparison between the incremental (symbols) and Green's function (line) estimation of (minus) the relative drain current variation $\Delta I_d/I_d$. Trap placed in the SiO$_2$ region.

3.4 Results

Following [51], where Monte Carlo simulation have been used to statistically describe the effect of RTN and RDF together, we have characterized the device variability extracting the slope $\lambda[mV/dec.]$ of the threshold voltage shift cumulative distribution. The cumulative distribution is calculated using the Green's function approach statistically. The $G_{D,\phi}$ has been extracted from Sentaurus Device simulation of the nominal device in threshold voltage condition and then we have randomly chosen one thousand of nodes at the Si-SiO$_2$ interface. To do this we had to increse the mesh density in that zones, but there aren't counter effects. So, we have calculated the drain current shift using eq. 3.7 multipling the value of $G_{D,\phi}$ on the selected nodes with the trapped charge that is the electron elementary charge. Using Y_{dg} we have been able to extract the threshold shift distribution, from the drain current shifts and one thousand of convolution integrals. Fig. 3.9 represents the example of the extraction of the slope of cumulative distribution for the nominal case, $Lg = 32$ nm $Tox = 0,8$ nm $Na = 2e18$ cm^{-3}, by mean of a linear interpolation implemented in MATLAB. The fitting is cut for higher value of ΔV_{th} which have a low probability.

From here on, we will use the parameter lambda λ to characterize variability and it's separated sources. The lambda parameter, or the slope of the cumulative distribution on a semi logarithmic graph, is chosen as a crucial parameter which allows to easily describe and compare the scaling trends due to different variability sources.

3.4.1 2D results

In this section we will analyse the results of RTN and RDF simulated on the 2D structure discribed in the paragraph 3.1 . In all the figures which follows the black line corresponds to RTN fluctuations only, the red line correspond only to RDF fluctuation and the blu line correspond to the total effect of RTN plus RDF. The number of sample used to extract the lambda is of one thousands. We want to stress the fact that we have only spent the run time of one simulation to calculate the Green's function and then made one thousands of product, the time needed is negligible in comparison to one thousand of simulations, to extract one value of lambda.

Fig. 3.10 shows the dependence of lambda on the oxide thickness. The reduction of the oxide thickness enhances the electrostatic control of the gate on the channel. The augmented control of the gate reduce the effect of both RDF and RTN, which show a reduction of nearly 70% in front of an oxide thickness reduction of 75% from the nominal value of $0,8$ nm.

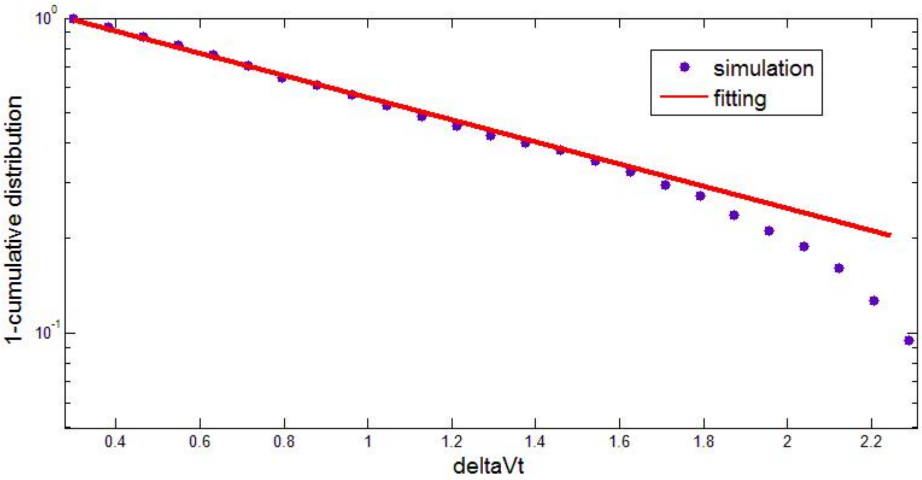

Figure 3.9: Extraction of the slope λ

Example of the evaluation of the slope $\lambda[mV/dec]$. The red line is the linear fitting of the cumulative distribution.

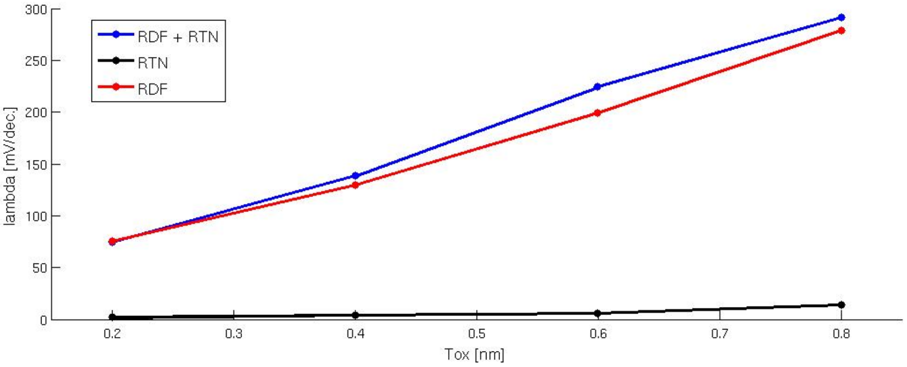

Figure 3.10: Lambda as a function of the oxide thickness

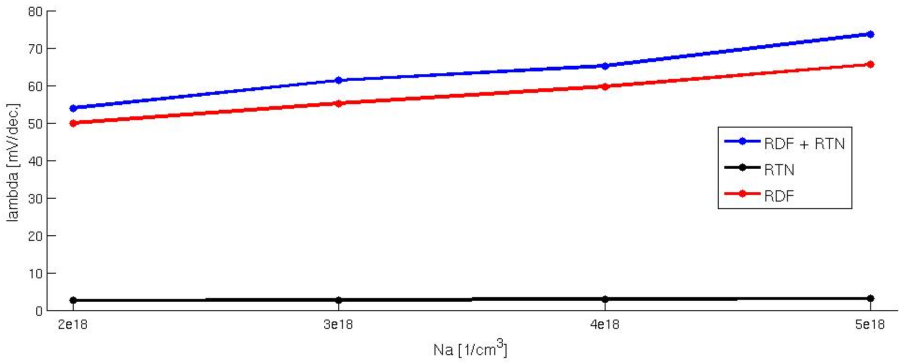

Figure 3.11: Lambda as a function of the substrate doping

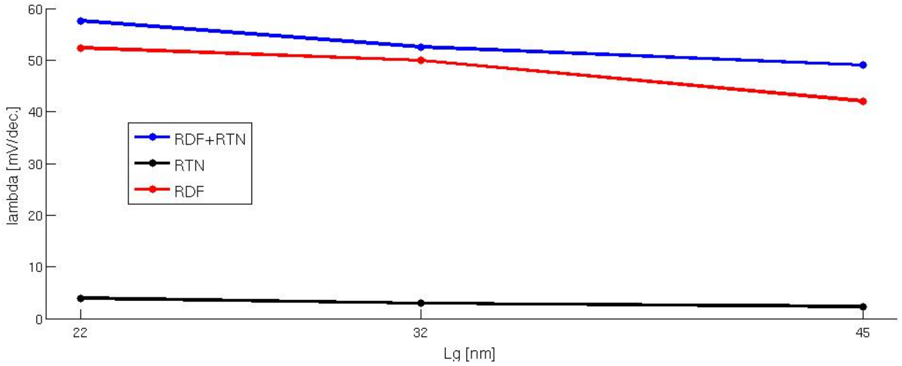

Figure 3.12: Lambda as a function of the gate length

Fig. 3.11 represents the dependence of lambda on the substrate doping. RTN doesn't present any effect while RDF show a small dependence. RDF is augmented of the 30% for a Na variation from the nominal value of $2e18$ cm^{-3} to $5e18$ cm^{-3}.
Fig. 3.12 doesn't show a strong dependence on gate length variations in both RDF and RTN for lambda.
In all the presented cases the the total effect is dominated by RDF, while RTN play a minor role.

3.4.2 3D results

In this section we will analyse the results of RTN and RDF simulated on the complete 3D structure discribed in paragraph 3.1 . In all the figures which follows the black line corresponds to only RTN fluctuations, the red line corresponds only to RDF fluctuation and the blu line correspond to the total effect of RTN plus RDF. The procedure is the

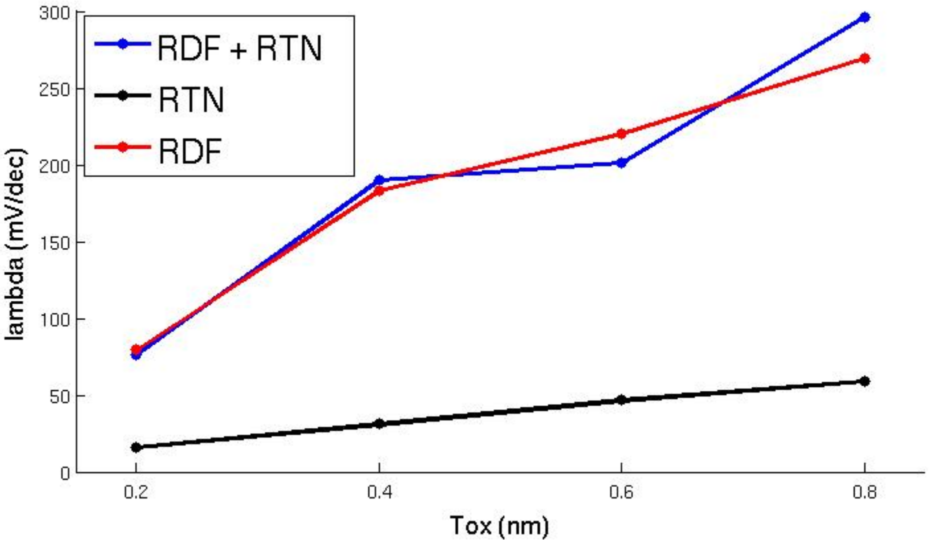

Figure 3.13: Lambda in function of the oxide thickness

same described in the above section.
As explained in paragraph 3.3, we have experienced some incoherence with the Green's function calculated by Sentaurus Device and the incremental to evaluate the effect of the trap on the drain current. The difference between the two approach is up to 50%. Despite this, the simulations have been repeated in the 3D case and due to the small variation caused by RTN compared to the variation caused by RDF the analysis is still reliable.

Fig. 3.13 shows the dependence of λ on the thickness oxide in the case of the 3D structure. The effect of the oxide thickness reduction is the same seen in the 2D structure despite the effects are stronger for every case.

Fig. 3.14 represents the dependence of λ on the substrate doping. In this case λ doesn't present any special dependence on the substrate doping variation. RTN show a linear dependence to the reduction of Na.

Fig. 3.15 shows the dependence of lambda on the gate length and also on the width that have the same value of Lg. The effect of RDF duplicate for from the 32 nm node to 22 nm.

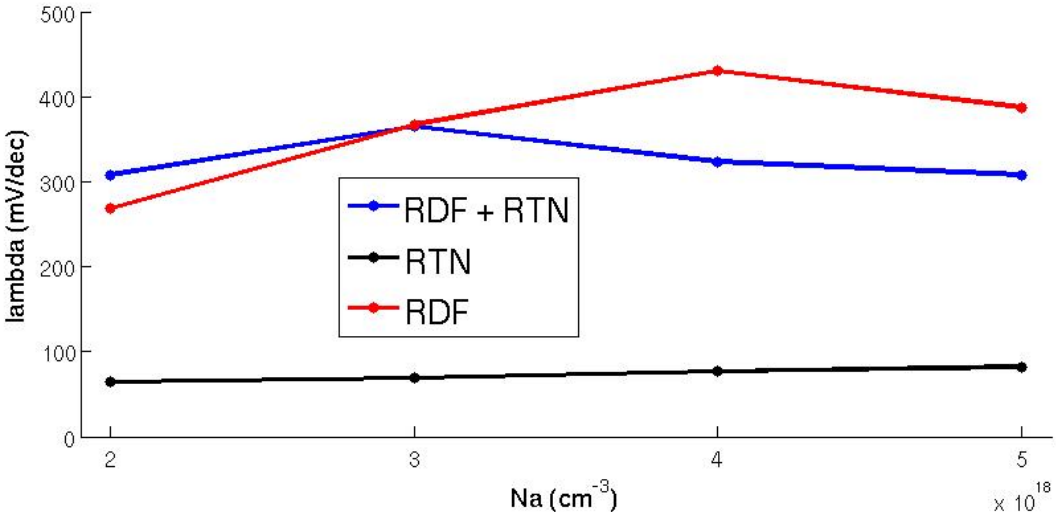

Figure 3.14: Lambda in function of the substrate doping

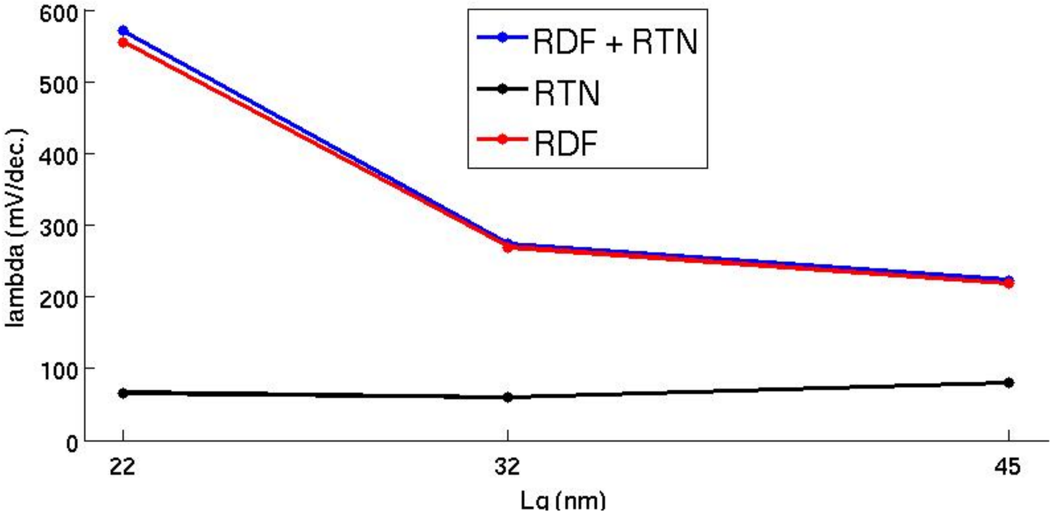

Figure 3.15: Lambda in function of the gate length

Chapter 4

Geometrical sensitivity

In the first chapter we have introduced the subject of device sensitivity analysis as a powerful tool for device optimization. The aggressive device scaling and the request of always better performances, in terms of consumption and realibility, requests higher attention to device design optimization. Due to insufficient accuracy of predictive tools set of simulations with a variety of geometry of the device under investigation are used. This approach requires large computational resources due to the large number of trials and the high number of grid points required.

In the framework of device sensitivity analysis as an optimization tool, we will describe as an example geometrical sensitivity analysis run with a novel and efficient Green's function approach. Geometrical sensitivity analysis accounts for random displacement interfaces, LER and LWR can also be included in this framework, and for deterministic variation of the geometry, e.g. field plate dimension. The geometrical optimization tool presented in this chapter can be used to do both the analysis described before, but, for time reasons, we have applyied it on the size optimization of a field plate FPMESFET. The application of a Field Plate on a MESFET enhanced the breakdown voltage characteristics [52], yielding it useful for power applications. The application of the FP technique is used also on HEMT [53], after its original proposal in the context of high voltage planar p-n junctions [54].

Power devices requirements

In the field of electric power conversion, transistors should behave as an ideal switch. High breakdown voltage and low energy losses are the most important requirements in power switching applications such as factory automation, telecommunications and

motor control [55]. The energy losses of a switching device are divided into static losses and dynamic losses. The static losses are the losses when the transistor is in the on-state and off-state. In the on-state a transistor should demonstrate very low on-resistance in order to decrease the conduction losses. In the off-state the transistor should behave as a perfect open but, inevitably, some leakage current flows. This leakage current should be very low in order to reduce the standby power consumption. The switching losses are due to the capacitance and the switching from the on-state to the off-state and vice versa which should be fast. Another requirement for the switching transistors is related to the passive elements such as capacitances, inductances and filters which form the power conversion system. By increasing the operation frequency, it is possible to reduce the size of the passive elements used, which results in a size reduction of the power conversion system. Therefore, the higher operation frequency is required as an important specification of a switching device.
Finally, the requirements for an electric power switching device can be summarized as follows:

- High blocking voltage, which expands the utilization field
- Low specific on-resistance, which reduces the device conduction losses
- Low capacitance, which reduces the switching losses and increases the operation frequency
- High operation frequency, which reduces the apparatus size

4.1 Theory

In [56] Gnudi et al. presented a sensitivity analysis technique for device design using a linearized method. In the following we give a brief review of this first linearized technique and then we will present our novel approach. Our study is based on 2D simulations, but the model is easily to extend to 3D simulations. For simplicity, we rewrite the drift-diffusion model 4.17 in the form

$$F_\phi(\phi, n, p; N_D, N_A, \Omega, A) = 0 \tag{4.1}$$

$$F_n(\phi, n, p; N_D, N_A, \Omega, A) = 0 \tag{4.2}$$

$$F_p(\phi, n, p; N_D, N_A, \Omega, A) = 0 \tag{4.3}$$

where 4.1 refers to Poisson equation, 4.2 and 4.3 refer to electron and hole continuity equations. ϕ, n, p are nodal values of the electric potential and of the carrier concentrations; N_A, N_D are the nodal values of the acceptor and donor impurity concetration, Ω and A are the cell areas and the cross-section to side-length ratios of a node, respectively. We have put in evidence geometrical variables because are necessary to explain the model.

Now assume that the device geometry is varied uniformly so that the mesh nodes undergo a small variation.

$$x_i = x_i^0 + \delta x_i \tag{4.4}$$

$$y_i = y_i^0 + \delta y_i \tag{4.5}$$

The choice of δx_i and δy_i is not unique. However, it is not critical as far as the mesh continue to well describe the device topology and the perturbation is small enoough to be linearized.

The change of nodes coordinate will modify the geometrical parameters Ω_i and A_{ij} as follows:

$$\Omega_i = \Omega_i^0 + \sum_{k=1}^{N_c} \left(\frac{\partial \Omega_i}{\partial x_k} \delta x_k + \frac{\partial \Omega_i}{\partial y_k} \delta y_k \right) \tag{4.6}$$

$$A_{ij} = A_{ij}^0 + \sum_{k=1}^{N_c} \left(\frac{\partial A_{ij}}{\partial x_k} \delta x_k + \frac{\partial A_{ij}}{\partial y_k} \delta y_k \right) \tag{4.7}$$

where N_c is the number of nodes excluding those at ohmic contacts. This changes induce variations to the electrical potential and carrier concentrations:

$$\phi = \phi^0 + \delta\phi \tag{4.8}$$

$$n = n^0 + \delta n \tag{4.9}$$

$$p = p^0 + \delta p \tag{4.10}$$

The system of equations 4.1 4.2 4.3 becames

$$F_\phi(\phi^0 + \delta\phi, n^0 + \delta n, p^0 + \delta p; N_D, N_A, \Omega + \delta\Omega, A + \delta A) = 0 \tag{4.11}$$

$$F_n(\phi^0 + \delta\phi, n^0 + \delta n, p^0 + \delta p; N_D, N_A, \Omega + \delta\Omega, A + \delta A) = 0 \tag{4.12}$$

$$F_p(\phi^0 + \delta\phi, n^0 + \delta n, p^0 + \delta p; N_D, N_A, \Omega + \delta\Omega, A + \delta A) = 0 \tag{4.13}$$

The above system can be linearized as follows:

$$\begin{bmatrix} \left(\dfrac{\partial F_\phi}{\partial \phi}\right)_0 & \left(\dfrac{\partial F_\phi}{\partial n}\right)_0 & \left(\dfrac{\partial F_\phi}{\partial p}\right)_0 \\ \left(\dfrac{\partial F_n}{\partial \phi}\right)_0 & \left(\dfrac{\partial F_n}{\partial n}\right)_0 & \left(\dfrac{\partial F_n}{\partial p}\right)_0 \\ \left(\dfrac{\partial F_p}{\partial \phi}\right)_0 & \left(\dfrac{\partial F_p}{\partial n}\right)_0 & \left(\dfrac{\partial F_p}{\partial p}\right)_0 \end{bmatrix} \begin{bmatrix} \delta\phi \\ \delta n \\ \delta p \end{bmatrix} = - \begin{bmatrix} \left(\dfrac{\partial F_\phi}{\partial \Omega}\right)_0 \\ \left(\dfrac{\partial F_n}{\partial \Omega}\right)_0 \\ \left(\dfrac{\partial F_p}{\partial \Omega}\right)_0 \end{bmatrix} \delta\Omega - \begin{bmatrix} \left(\dfrac{\partial F_\phi}{\partial A}\right)_0 \\ \left(\dfrac{\partial F_n}{\partial A}\right)_0 \\ \left(\dfrac{\partial F_p}{\partial A}\right)_0 \end{bmatrix} \delta A \tag{4.14}$$

The left hand side of the system is the Jacobian of the system which is already available since it is used in Newton Method to solve the system equation in nominal conditions. Hence, to find the parameters variations $\delta\phi$, δn and δp only the assembly of the right hand side of the system and one back substitution are required.
Summarizing, the variations of a geometrical paramters like the oxide thickness, induce variation in the three mains physicals variables ϕ, n and p that can be evaluated linearising the variation and calculating the right hand side of the system 4.14. This last is composed by geometrical parameters variations.
Following Gnudi et al. [56] where the authors calculate the geometrical sensitivity, variation of an electrical parameter in function of a geometrical variation, through the cell area and cross-section derivative. Instead, we use the Green's function formulation of the local sensitivity, to calculate the geometrical sensitivity.

4.2 Green's function based method for geometrical sensitivity

Numerical device simulation is performed by solving the discrete Drift-Diffusion model, eq. 4.17, which can be written in implicit mode as follow

$$F_\phi(\phi, n, p, x_i, y_i) = 0 \quad \text{Poisson Eq.} \tag{4.15}$$

$$F_n(\phi, n, p, x_i, y_i) = 0 \quad \text{Electron continuity Eq.} \tag{4.16}$$

$$F_p(\phi, n, p, x_i, y_i) = 0 \quad \text{Hole continuity Eq.} \tag{4.17}$$

where ϕ, n and p are, respectively, the discrete potential and carrier concentration distribution inside the device and $\{x_i, y_i\}$ are the 2D node coordinates. In reality the descritized equations depends on the ratio of bi secants and edges $\{D_ij/l_ij\}$ and on the cells areas eq. 4.1, see Fig. 2.1. In the numerical and Green's function formulation is not necessary to do any assumption and so we consider the generic dependence on 2D node coordinates. So, if we assume to make a small variation in the device geometry

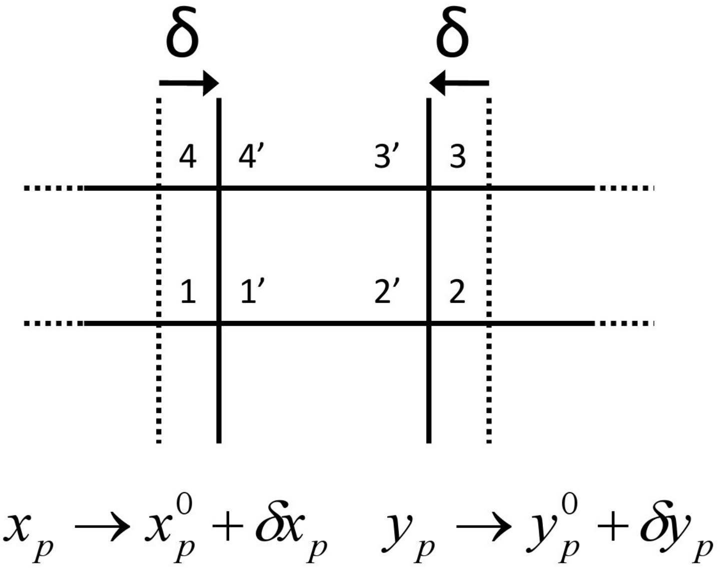

Figure 4.1: Proportional variation of the mesh points
Rectmesh allow to proportionally varies the node coordinates when the mesh is shrink or stretch

(to perturbed the geometry) so that the corresponding mesh is always valuable, and this is possible only with a small variation of the nodal coordinates, we can write the novel coordinates (the perturbed coordinates) as

$$x_p = x_i^0 + \delta x_i, \qquad y_i = y_i^0 + \delta y_i \tag{4.18}$$

where δx_i and δy_i are the small node variations which has to maintain the validity of the grid on the geometry. We can enlarge a region of the device, moving all the nodes so that they move uniformly, see 4.1. In the MATLAB function that we use, part of the in-house code POLITO FBZ, this procedure is automatically done by the grid generator, *rectmesh.m*. We vary the length of the region and re-compute the mesh maintaining the same division number in the region and so the grid maintain the same proportion, numeration and structure of the old nodes, but it results more stretched along the direction of the geometry variation.

Corresponding to small variation in the geometry we have small variation of the physical parameters

$$\phi = \phi^0 + \delta\phi, \qquad n = n^0 + \delta n, \qquad p = p^0 + \delta p \tag{4.19}$$

where $\delta\phi$, δn and δp are small-change variations.
We can now rewrite the 4.15 of the Drift-Diffusion model as

$$F_\phi(\phi^0 + \delta\phi, n^0 + \delta n, p^0 + \delta p, x_i^0 + \delta x_i, y_i^0 + \delta y_i) = 0 \tag{4.20}$$

$$F_n(\phi^0 + \delta\phi, n^0 + \delta n, p^0 + \delta p, x_i^0 + \delta x_i, y_i^0 + \delta y_i) = 0 \tag{4.21}$$

$$F_p(\phi^0 + \delta\phi, n^0 + \delta n, p^0 + \delta p, x_i^0 + \delta x_i, y_i^0 + \delta y_i) = 0 \tag{4.22}$$

For simplicity in the rest of the text we take as example the Poisson equation, but the same can be done for the carrier continuity equation easily.
If we linearize the Poisson equation around the nominal physical value (physical values of the unperturbed system), we approximatively obtain

$$\begin{aligned} & F_\phi(\phi^0, n^0, p^0, x_i^0, y_i^0) + \cdots \quad 1^{st} \text{ term} \\ \left.\frac{\partial F_\phi}{\partial \phi}\right|_0 \delta\phi + \left.\frac{\partial F_\phi}{\partial n}\right|_0 \delta n + \left.\frac{\partial F_\phi}{\partial p}\right|_0 \delta p + \left.\frac{\partial F_\phi}{\partial x_i}\right|_0 \delta x_i + & \left.\frac{\partial F_\phi}{\partial y_i}\right|_0 \delta y_i = 0 \quad 2^{nd} \text{ term} \end{aligned} \tag{4.23}$$

The first term is the equation evaluated with the unperturbed parameters, 0^{th} order, and is zero for assumption while the others are the perturbed terms and can be divided in two groups as illustrated in the follow equation.

$$\left.\frac{\partial F_\phi}{\partial \phi}\right|_0 \delta\phi + \left.\frac{\partial F_\phi}{\partial n}\right|_0 \delta n + \left.\frac{\partial F_\phi}{\partial p}\right|_0 \delta p = -\left.\frac{\partial F_\phi}{\partial x_i}\right|_0 \delta x_i - \left.\frac{\partial F_\phi}{\partial y_i}\right|_0 \delta y_i \tag{4.24}$$

The terms on the left are the Jacobian of the Poisson equation evaluated with the nominal physical parameters and without grid variation terms. The terms on the right represent the variations of the Poisson equation due only to the grid variation with the nominal physical values. This term is equivalent to the right hand terms in 4.14 which represent geometrical variation through cell areas and cross-section. These terms are the consequence of the residual variation of the Poisson equation calculated with the nominal physical values.

$$\Delta RHS = F_\phi(\phi^0, n^0, p^0, x_i^0 + \delta x_i, y_i^0 + \delta y_i) - F_\phi(\phi^0, n^0, p^0, x_i^0, y_i^0) \tag{4.25}$$

The last term of the equation is zero for assumption and the first term is easy to be extracted with the following alghorithm:

a calculate the system solution at the working point of interest with a Newton method. At the end you will have a Jacobian matrix and the values of the main variables ϕ^0, n^0 and p^0 that make $F_\phi(\phi^0, n^0, p^0, x_i^0, y_i^0) = 0$. In this case the residual is zero.

b modify the geometry

c move the mesh to fit the novel geometry

d re-assemble the Jacobian matrix with the physical parameters calculated in the first step to the new mesh points. In this case the residual is different from zero and the variations is due to the geometry variation.

So we can write:

$$\frac{\partial F_\phi}{\partial \phi}_0 \delta\phi + \frac{\partial F_\phi}{\partial n}_0 \delta n + \frac{\partial F_\phi}{\partial p}_0 \delta p = -F_\phi(\phi^0, n^0, p^0, x_i^0 + \delta x_i, y_i^0 + \delta y_i) = \Delta RHS \quad (4.26)$$

We have demonstrated how the perturbation induced by the perturbed coordinates can be easely evaluated through the residual variation induced by the application of the Jacobian to the modify mesh.
Now, we are able to calculate the effect of the geometric pertubation to the device terminal characteristics using the Green's function G_α where α is a given terminal observable. The Green's function has to be extracted from the nominal device at the working point of interest, which must be the same used for the Jacobian evaluation descripted above.
Toghether with the Green's function we can evaluate the perturbation on the device terminal

$$\delta\alpha = -\int_\Omega G_\alpha F_\phi d\sigma = \sum_{i-node} G_{i,\alpha} F_{i,\phi} A_i = \sum_{i-node} G_{i,\alpha} \Delta RHS_i \quad (4.27)$$

where α is terminal observable, Ω is the device volume, A_i is the control area of the i-esimo node and ΔRHS_i is the residual of the i node.

4.3 Case Study

4.3.1 Field Plate MESFET

We have tested our method on a Field Plate (FP) MESFET, see Fig. 4.2 . FP technology employed on GaAs metal-semiconductor fiel effect transistor FPFET, where the field-modulating plate FP, whose potential is kept equal to that of the Schottky gate, or of source/drain, is placed on the passivation film between the gate and the drain recess edge, has been extensively exploited to improve the device breakdown voltage > 40 V and microwave power performance at high drain voltages > 20 V [57].

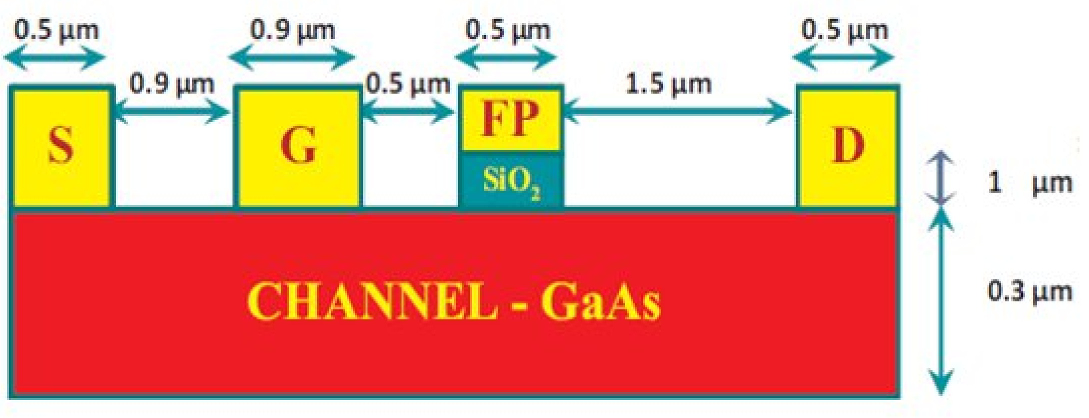

Figure 4.2: Field Plate MESFET structure

Field PLate solutions have been extensively exploited to improve the device breakdown voltage. This structure is a perfect example how geometrical sensitivity is a powerful tool for device optimization.

The presence of the field plate impairs RF device features, thus requiring a trade off between breakdown voltage and device speed defined under terms of FP design such as oxide physical dimensions (thickness, length, bias etc.). In this respect, the availability of simulation tools with geometric sensitivity capabilities would widely improve the fine tuning of the device design, and in principle should allow for automated device optimization through gradient-based techniques.
The tested structure is a standard GaAs FPMESFET with a FP as represented in figure 4.2. The Gate length is $Lg = 0.9$ μm whith a distance of 2.5 μm from the drain and 0.9 μm from the source. The layer is GaAs film thick 0.3 μm and n-type doped $2e17$ cm^{-3}. An FP electrode is placed on the dielectric film of SiO$_2$, thick 1 μm, between the gate and the drain edge. We define three important FP parameters: L_{FP}, L_{FG} and Tox , which are the FP length, the FP distance from the gate and the SiO$_2$ thickness under FP, respectively. The device output characteristics with and without FP are shown in Fig. 4.3 and show how the presence fot he field plate doubled the brakdown voltage V_{br}.

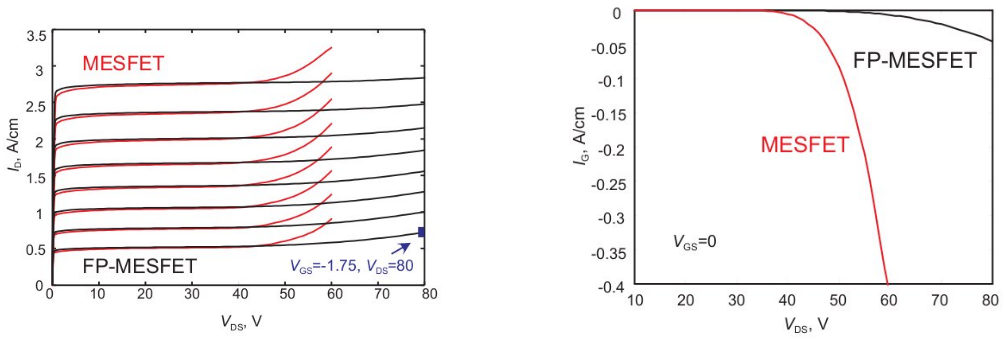

(a) Id vs Vd

(b) Ig vs Vd

Figure 4.3: MESFET vs FPMESFET characteristic
Device output characteristics with and without FP are shown. The presence of the Field Plate doubled the breakdown voltage.

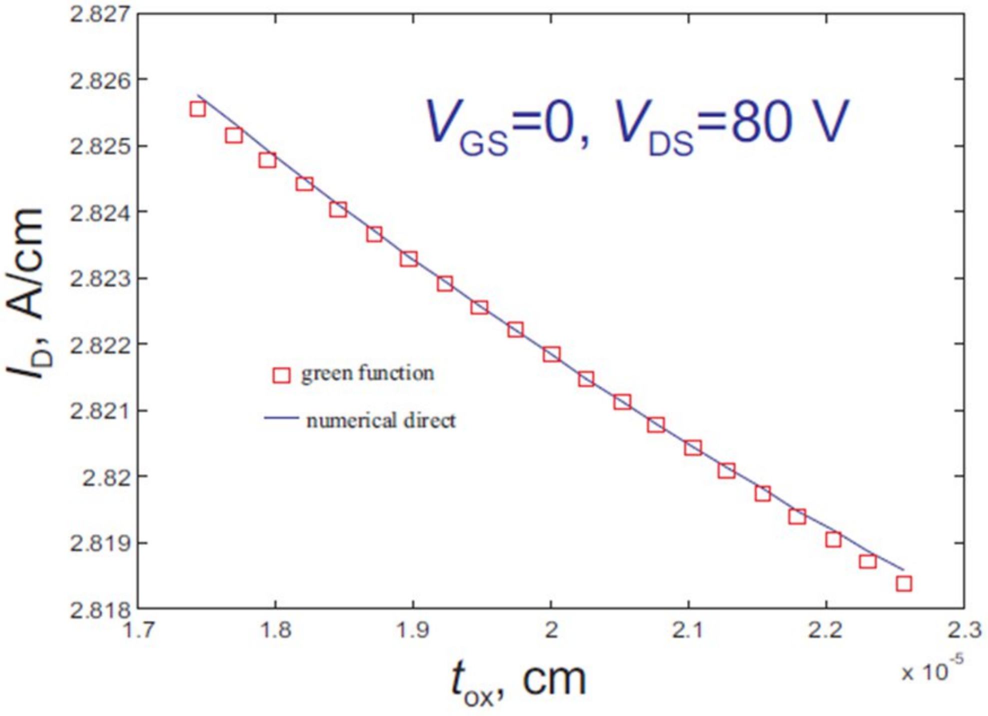

Figure 4.4: Geometrical sensitivity validation
Comparison between the incremental approach of simulate every oxide thickness and the Green’s function approach obtained in one simulation.

4.3.2 Model Validation

The Green's function technique was applied in order to monitor the variation of the drain current at the onset of breakdown conditions, see mark in Fig. 4.3(a), as a function of the FP thickness, FP length and FP distance from gate electrode.
The Green's function approach has been validated on the FPMESFET described in the above section using the in-house code described in 2.3.2 including avalanche generation. The electric field dependence of the electron and hole ionization coefficients was included by fitting the measurements by Bulman [58]. This code was complemented with the Green's function sensitivity analysis both in small signal and large-signal conditions. Figure 4.4 represent the comparison between incremental and the linearized Green's function approach concerning the drain current Id in function of oxide thickness Tox variations. The direct numerical approach consist in running simulations for every oxide thickness of interest and compute the relative drain current variations. The agreement between the two methods is good and the linearized approach was accurate up to $15-20\%$ variation of the geometrical parameters with respect to nominal values. This mean that the physical variable variations induced by geometrical variations are small enough to be linearised and that our method can be used to run geometrical sensisitivty analysis.

4.3.3 Analysis of the results

Field Plate length variations

Figures 4.5(a) and 4.5(b) show, respectively, the variations of the drain and gate current as a function of the FP length variation. It is clearly seen that the sensitivity is much lower for FP length higher than 1 μm. Further increase of the FP length does not lead to significant reduction in the drain avalanche current.

Oxide Thickness variations

Figures 4.6(a) and 4.6(b) show, respectively, the variations of the drain and gate current as a function of the field plate oxide thickness. The trend is the same of L_{FP} where the sensitivity is much lower for oxide thickness higher than 1 μm.

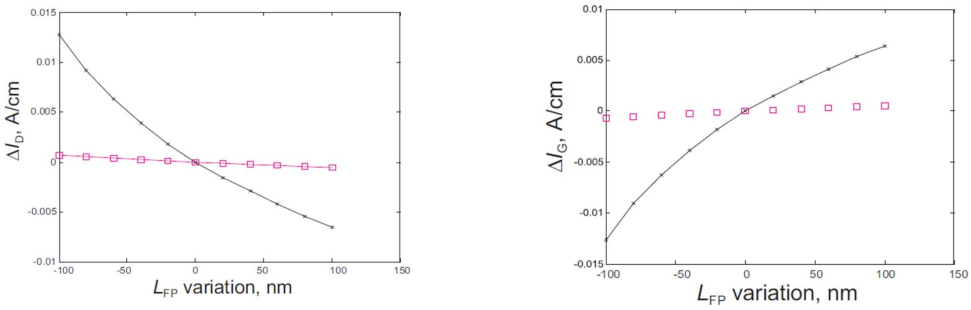

(a) Id vs L_{FP} (b) Ig vs L_{FP}

Figure 4.5: Id and Ig versus field plate length

The black line refers to variations of the FP around the nominal value of $0, 6$ μm. The red squares refers to variations of the FP around the nominal value of $1, 4$ μm. The drain and gate current is calculate in breakdown conditions.

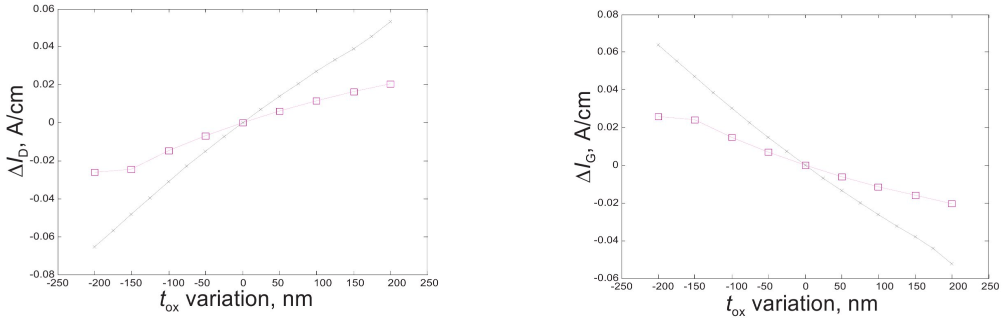

(a) Id vs L_{FP} (b) Ig vs L_{FP}

Figure 4.6: Id and Ig versus xide thickness variations

The black line refers to variations of the FP around the nominal value of $0, 8$ μm. The red squares refers to variations of the FP around the nominal value of $1, 2$ μm. The drain and gate current is calculate in breakdown conditions.

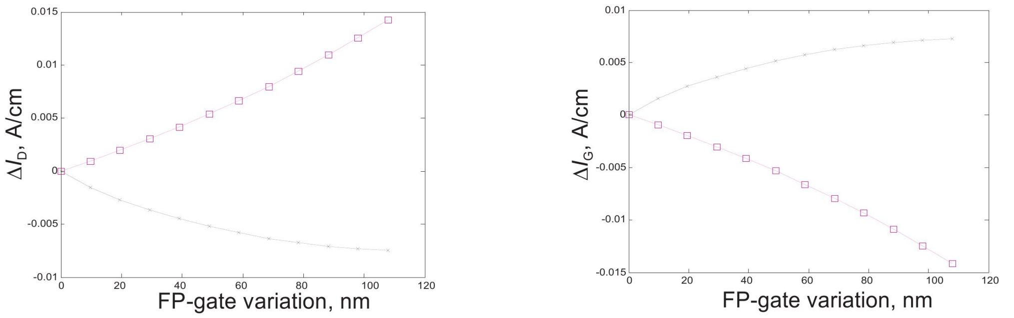

(a) Id vs L_{FP}

(b) Ig vs L_{FP}

Figure 4.7: Field Plate distance from gate variations
The black line refers to variations of the FP around the nominal value of $0,5$ μm. The red squares refers to variations of the FP around the nominal value of $0,8$ μm. The drain and gate current is calculate in breakdown conditions.

Field Plate distance from gate variations

Figures 4.7(a) and 4.7(b) shows, respectively, the variations of the drain and gate current as a function of the distance between gate and field plate. Results shows that for a positive variation of this parameter around a nominal value of 0.5 μm, the sensitivity of the drain current is negative (and the opposite holds for the gate current): this means that by further separting the gate and FP contacts the FP effect is enhanced and the breakdown current decreases. On the other hand for a nominal value of 0.8 μm the sensitivity sign is changed, thus suggesting that an optimum value of this parameter can be found at an intermediate value of the gate-FP distance. Notice however that the sensitivity absolute value is lower than in the other two cases.

In such simulations a direct link has been established between the breakdown condition and the device geometry. Despite similar simulation efforts have been demonstrated in previous works both for GaAs and GaN FETs [52] [53], such papers show that a direct analysis of device performances in breakdown conditions is extremely numerically intensive. On the contrary, the proposed approach, based on the linearization of the device equations with respect to mesh variations allows for a dramatic reduction of simulation time.

Appendix A

Mesh Generator and the mesh problem

Creating a mesh is the first step in a wide range of applications, including scientific computing and computer graphics. Here we want to dicuss the mesh problem for finite element method used in electron device simulations.
Grid generators must be based both on geometrical and numerical considerations. Some general guidelines can be suggested in order to minimize the discretization error, produced in the passage from continuos algebra to discrete systems. I have found some guidelines in articles and book which discuss about mesh:

- The grid should accourately describe the device topology, considering also impurity profiles and other critical zones for the main variables (potential, local charge, recombination etc.)
- the grid should vary as smoothly as possible because the local truncation error is proportional to node distance
- the presence of angles above 90 must be minimized and the minimum interior angle should be maximized in order to have well conditioned matrices
- whenever possible, element edges should be aligned to the direction of current flow
- in case of a triangular grid, equilateral triangles are preferred
- for computational reasons, the mesh should have small elements to resolve the fine details of the geometry, but larger sizes where possible, to reduce the total number of nodes

Many different mesh generation algorithms have been developed, and some of the most popular ones are described in the surveys by Bern and Plassmann [59] and Owen [60].

In the following we will discribe the two mesh genrator that I have used and modified in order to improve the performances of the in-house code discribed in the thesis.

Rectmesh

Rectmesh is a simple 2D meshgenerator included in the in-house code POLITOFBZ which allows to create a triangular mesh after dividing the domain in rectangular elements. After dividing the total domain in rectangular region, the user must set a division number for the direction x and y for every region. The matlab code to generate the node takes only few lines and is:
$fork = 1 : length(geom.div_x),$
$x(index : sum(geom.div_x(1 : k)) + 1) = linspace(xb(k), xb(k + 1), geom.div_x(k) + 1);$
$index = index + geom.div_x(k); end$
$index = 1;$
$fork = 1 : length(geom.div_y),$
$y(index : sum(geom.div_y(1 : k)) + 1) = linspace(yb(k), yb(k + 1), geom.div_y(k) + 1);$
$index = index + geom.div_y(k); end$
$mesh.xgrid = x; mesh.ygrid = y;$
where geom.div is an array with division number for every device region and xb and yb are the coordinates that define the region boundaries.
With this data it is easy to extract the nodes coordinates which form a rectangular grid. This rectangular grid can be easly tranformed into a right triangular grid defining one more edge for every rectangle.
Figure 8 shows an example of a mesh generated with rectmesh for a p-n junction. In theory there's must be a higher density node at the junction and the mesh must smoothly relaxes as more is far from the junction. The figure shows that an high density of nodes can be set near the junction, but the mesh doesn't relax smoothly and there are also many nodes far from the junction. Despite, in theory, this is not a good mesh, the solution is in agreement with other simulators. This is probably due to Newton alghorithm which is very powerful and can solve also some mesh defects without lossing in reliability and performances.
The principal problem of this type of mesh remains the high number of nodes in region where are not necessary and if in 2D simulations the problem is acceptable, in 3D it will create a very large number of nodes where are not necessary. In the end, rectmesh,

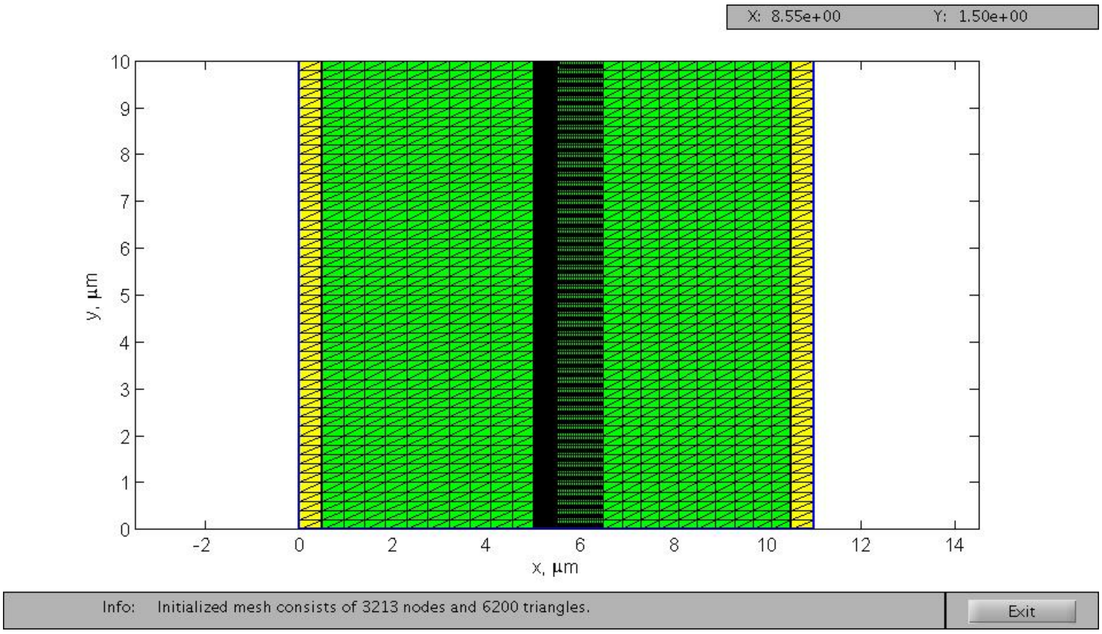

Info: Initialized mesh consists of 3213 nodes and 6200 triangles.

(a) Rectmesh p-n junction

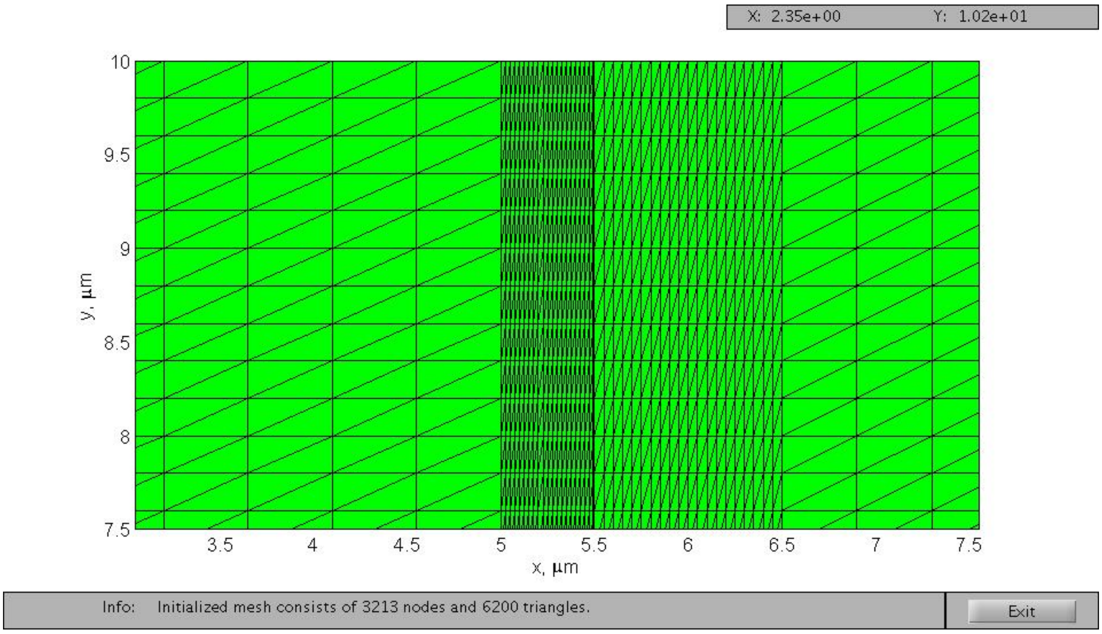

Info: Initialized mesh consists of 3213 nodes and 6200 triangles.

(b) Rectmesh p-n junction zoom

Figure 8: Rectmesh p-n junction

(a) shows an example of a mesh generated by rectmesh on a p-n junction (b) shows a zoom of (a) in the junction zone is a simple and efficient meshgenerator for 2D simulations, but can't be applied in 3D simulations.

Trimesh

Persson et al. present in [61] a simple mesh generators implemented in Matlab and easy to extend for any purpose. The authors want to fill the lack in the use of mesh generators which, normally, tend to be black boxes and I agree with that assumption. For this purpose they have created a simple algorithm for mesh generation that we have modified to be adopted in our in house simulator.
The proposed algorithm implements an iterative technique based on the physical analogy between a simplex mesh and a truss structure. Meshpoints are nodes of the truss. Assuming an appropriate force-displacement function for the bars in the truss at each iteration, we solve for equilibrium. The two essential steps are the nodes displacement under the bar forces and the Delaunay triangulation algorithm that adjusts the topology defining the edges. The resulting mesh is surprisingly well-shaped.
Without goin into the details because we want to present the general algorithm and the results obtained.

The algorithm

In this section we will explain the 2D algorithm, but it can be easely expanded to the 3D case. In the plane any set of points can be triangulated by the Delaunay algorithm [62]. In the physical model, the edges of the triangles (the connections between pairs of points) correspond to bars, and the points correspond to joints of the truss. Each bar has a force-displacement relationship $f(l, l_0)$ where l is the current bar lenght and l_0 is its unextended length.
The positions of the joints are our principal unknowns and are found by solving for a static force equilibrium in the structure. To solve for the force equilibrium, collect the nodes coordinates of all meshpoints into an p:

$$p = [x, y] \tag{28}$$

The force vector $F(p)$ has horizontal and vertical components at each meshpoint:

$$F(p) = [F_{int,x}(p) F_{int,y}(p)] + [F_{ext,x}(p) F_{ext,y}(p)] \tag{29}$$

where F_{int} contains the internal forces from the bars, and F_{ext} are the external forces (reactions from the boundaries). The first column of F contains the x-components of the forces, and the second column contains the y-components.

Note that $F(p)$ depends on the topology of the bars connecting the joints given by the Delaunay triangulation of the meshpoints. The Delaunay algorithm determines non-overlapping triangles that fill the convex hull of the input points, such that every edge is shared by at most two triangles, and the circumcircle of every triangle contains no other input points. In the plane, this triangulation is known to maximize the minimum angle of all the triangles. The force vector $F(p)$ is not a continuous function of p, since the topology is changed by Delaunay as the points move at every iteration.

The system $F(p) = 0$ has to be solved for a set of equilibrium positions p. This is a relatively hard problem, partly because of the discontinuity in the force function and partly because of the external reaction forces at the boundaries.

A simple approach to solve $F(p) = 0$ is to introduce an artificial discretized time-dependence. At the discretized time $t_n = n\Delta t$, the approximate solution $p_n \approx p(t_n)$ is updated by

$$p_{n+1} = p_n + \Delta t F(p_n) \tag{30}$$

This means that the force F is applied to mesh structure for a time Δt moving the nodes from the position p_n to p_{n+1}. When evaluating the force function, the positions p_n are known and therefore also the truss topology. The external reaction forces enter in the following way: All points that go outside the region during the update from p_n to p_{n+1} are moved back to the closest boundary point. This conforms to the requirement that forces act normal to the boundary. The points can move along the boundary, but not go outside.

There are many alternatives for the force function $f(l, l_0)$ in each bar. Good results can be obtained with piecewise linear force as

$$f(l, l_0) = \begin{cases} (l - l_0) \text{ for } l < l_0 \\ 0 \text{ for } l \geqslant l_0 \end{cases} \tag{31}$$

The proposed treatment of the boundaries means that no points are forced to stay at the boundary, they are just prevented from crossing it. It is therefore important that most of the bars give repulsive forces $f > 0$, to help the points spread out across the whole geometry. This means that $f(l, l_0)$ should be positive when is near the desired length, which can be achieved by choosing l_0 slightly larger than the length we actually desire. The desired edge length distribution is provided by the user as an element size function $fh(x, y)$. Note that h$fh(x, y)$ does not have to equal the actual size; it gives the relative distribution over the domain. This avoids an implicit connection with the number of nodes, which the user is not asked to specify. $fh(x, y)$ could also be created using

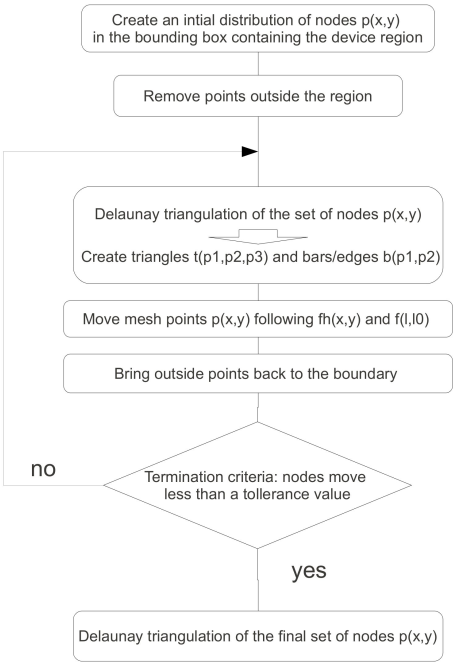

Figure 9: Schematic repprensentation of the Trimesh algorithm
The scheme represent a schematic repprensentation of the Trimesh orginal algorithm. This flow is the core function of the mesh generator. The complete original source code is added at the end of this chapter.

adaptive logic to follow physical quantities variations in the device, e.g. the electric field.
The initial node positions p_0 can be chosen in many ways. A random distribution of the points usually works well, but when a non-uniform size distribution is desired, the convergence is faster if the initial distribution is weighted by probabilities proportional to $1/fh(x,y)^2$ which represent the density.

Implementation

Figure 9 repprensent a schematic repprensentation of the principal step contained in the core function of the original algorithm. In order to adapt the meshgenerator to POLITOFBZ wrap functions have been created to manage input and output data. A few options have been added in order to optimize the feature of the mesh to the use in device simulations, i.e. density gradient applyied to $fh(x,y)$ in order to obtain smoother meshes.

The core alghorithm starts with the generation of a random distribution of points p_0 that can follow the the density of nodes reppresented by $1/fh(x,y)^2$ or any other distribution of interest. The points can be generated in a box greater than the device geometry. This feature can be useful for non regulare geometry, i.e. ringa, or for moving boundaries analysis. Points outside the device are removed. Once created a first point distribution the main loop starts. First, we use the Delauny algorithm implemented in Matlab which gives as results triangles and bars. At this step we have to calculate the difference between the actual bar lenghts and the one described in fh. With the difference we can calculate the force to apply at each node. Once the nodes are moved by the force we have to bring back points that gone outside the device region. At this point we apply a termination criterion. Normally, the loop finishes when all interior nodes moved less than tollerance set from the user. If the criteria is not matched the loop restarts from the delaunay triangulation of the new points, else the loop stops. This algorithm gives back to the user a set of points that can be triangulated with the Delaunay algorithm resulting in a mesh strucutre.

Results of Trimesh

The meshes generated by Trimesh are high quality meshes with many triangles almost equilateral. A first test has been made using as fh a 2D cosine, where we want to have a high density of nodes on the cosine. Figure 10(a) show the fh function of a 2D cosine. The fh function is defined by the user and is foundamental to obtain a well shaped mesh which discrebed the device topology. With the fh showed in 10(a) the mesh 10(b) is obtained. The resulting mesh is of high quality, with an high density of nodes on the cosine which varies smoothly.

To obtain a mesh which varies so smoothly we have also implemented a gradient limiting function which act on fh imposing a maximum gradient defined by the user.

Once tested the mesh generator, we have applied it on a p-n junction and linked it with POLITOFBZ. Figure 11 shows the mesh and the potential calculated on it of a p-n junction. Despite the high quality of the mesh no further improvement has been seen compared to the use of rectmesh. The number of iteration step and solution doesn't vary. On the contrary, the mesh generated with trimesh has a larger number of nodes. The Trimesh algorithm is a very good mesh generator, but need further improvement to be used in device simulation. Probably it will be more efficient in 3D simulations.

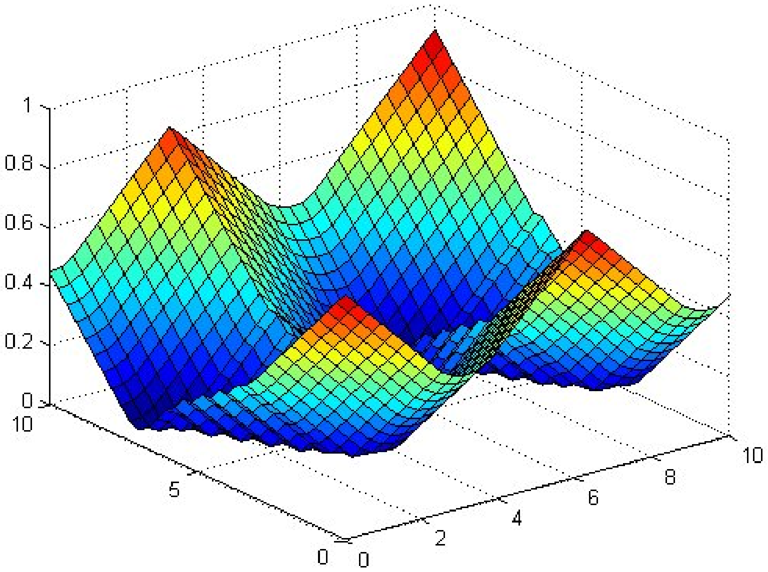

(a) fh cosine function

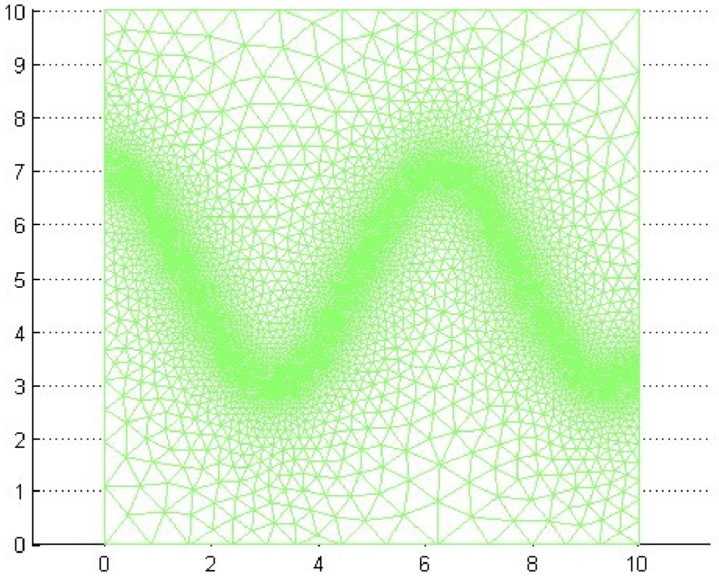

(b) Cosine mesh

Figure 10: Trimesh example of a cosine mesh

(a) shows an fh function of a 2D cosine mesh obtained using density gradient algorithm to smooth the mesh (b) the mesh generated with the fh represented in (a)

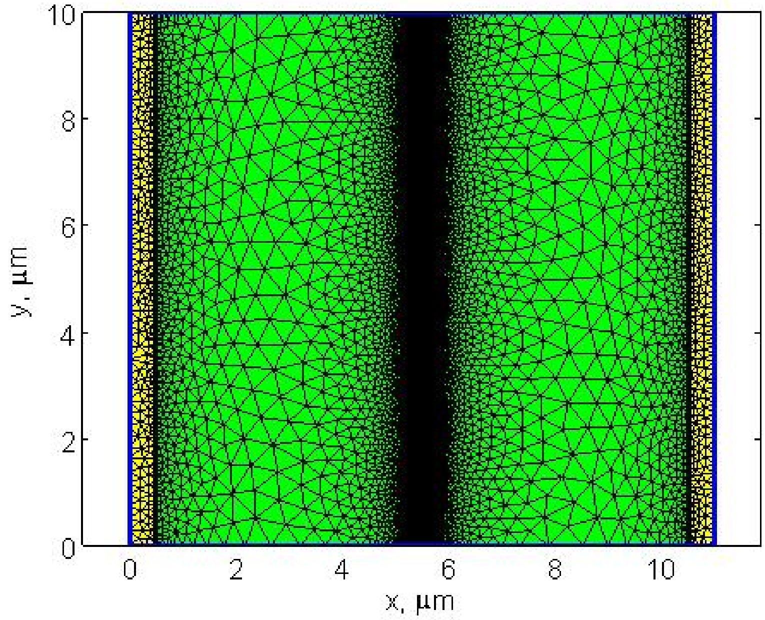

(a) Trimesh example of p-n junction - Mesh

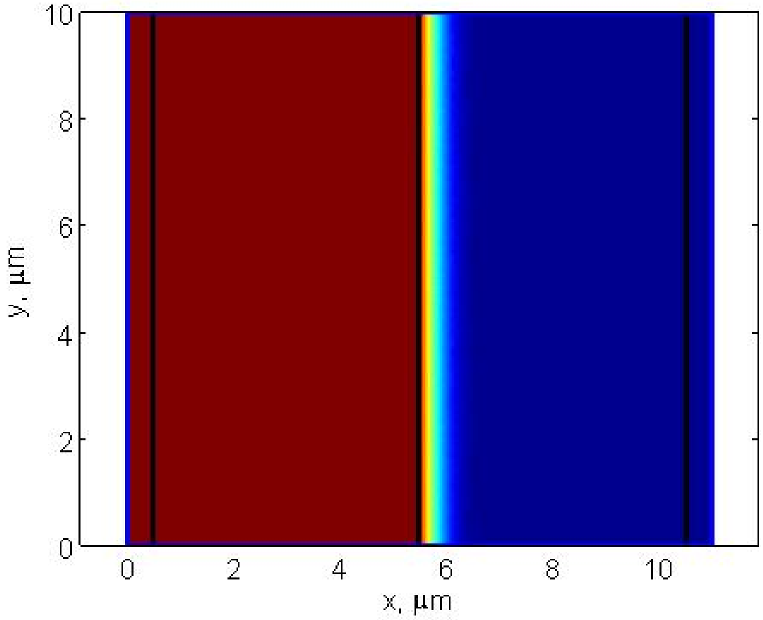

(b) Trimesh example of p-n junction - Potential

Figure 11: Trimesh example of a p-n junction

(a) shows the mesh of a p-n junction obtained with Trimesh (b) shows the potential of the p-n junction obtained with the mesh (a)

Original Trimesh code

Here we reported the original Matlab code as written in [61] where the function is called *distmesh2d*.

```
function [p,t]=distmesh2d(fd,fh,h0,bbox,pfix,varargin)
dptol=.001; ttol=.1; Fscale=1.2; deltat=.2; geps=.001*h0;
deps=sqrt(eps)*h0;
% 1. Create initial distribution in bounding box
[x,y]=meshgrid(bbox(1,1):h0:bbox(2,1),
bbox(1,2):h0*sqrt(3)/2:bbox(2,2));
x(2:2:end,:)=x(2:2:end,:)+h0/2; % Shift even rows
p=[x(:),y(:)]; % List of node coordinates
% 2. Remove points outside the region, apply the rejection method
p=p(feval(fd,p,varargin{:})<geps,:); % Keep only d<0 points
r0=1./feval(fh,p,varargin{:}).^2; % Probability to keep point
p=[pfix; p(rand(size(p,1),1)<r0./max(r0),:)]; % Rejection method
N=size(p,1); % Number of points N
pold=inf; % For first iteration
while 1
% 3. Retriangulation by the Delaunay algorithm
if max(sqrt(sum((p-pold).^2,2))/h0)>ttol % Any large movement?
pold=p; % Save current positions
t=delaunayn(p); % List of triangles
pmid=(p(t(:,1),:)+p(t(:,2),:)+p(t(:,3),:))/3; % Compute centroids
t=t(feval(fd,pmid,varargin{:})<-geps,:); % Keep interior triangles
% 4. Describe each bar by a unique pair of nodes
bars=[t(:,[1,2]);t(:,[1,3]);t(:,[2,3])]; % Interior bars duplicated
bars=unique(sort(bars,2),â€™rowsâ€™); % Bars as node pairs
% 5. Graphical output of the current mesh
trimesh(t,p(:,1),p(:,2),zeros(N,1))
view(2),axis equal,axis off,drawnow
end
% 6. Move mesh points based on bar lengths L and forces F
barvec=p(bars(:,1),:)-p(bars(:,2),:); % List of bar vectors
L=sqrt(sum(barvec.^2,2)); % L = Bar lengths
```

```
hbars=feval(fh,(p(bars(:,1),:)+p(bars(:,2),:))/2,varargin{:});
L0=hbars*Fscale*sqrt(sum(L.^2)/sum(hbars.^2)); % L0 = Desired lengths
F=max(L0-L,0); % Bar forces (scalars)
Fvec=F./L*[1,1].*barvec; % Bar forces (x,y components)
Ftot=full(sparse(bars(:,[1,1,2,2]),ones(size(F))*[1,2,1,2],
[Fvec,-Fvec],N,2));
Ftot(1:size(pfix,1),:)=0; % Force = 0 at fixed points
p=p+deltat*Ftot; % Update node positions
% 7. Bring outside points back to the boundary
d=feval(fd,p,varargin{:}); ix=d>0; % Find points outside (d>0)
dgradx=(feval(fd,[p(ix,1)+deps,p(ix,2)],varargin{:})-d(ix))/deps;
dgrady=(feval(fd,[p(ix,1),p(ix,2)+deps],varargin{:})-d(ix))/deps;
% Project back to boundary
p(ix,:)=p(ix,:)-[d(ix).*dgradx,d(ix).*dgrady];
% 8. Termination criterion:
%All interior nodes move less than dptol (scaled)
if max(sqrt(sum(deltat*Ftot(d<-geps,:).^2,2))/h0)<dptol, break; end
end
```

Appendix B

Sentaurus Command Files

Sentaurus Device IdVg sweep

```
Device NMOS {

Electrode {
     { name="Source" voltage= 0.0 }
     { name="Drain"  voltage= 0.0 }
     { name="Bulk"   voltage= 0.0 }
#if @< [string compare Poly @Poly_or_Elec@] >@ == 0
     { name="FGate"  voltage= 0.0 }
#else
     { name="FGate"  voltage= 0.0 barrier=-0.55}
#endif
}

File {
        Grid    = "@tdr@"

        Current = "@plot@"
        Plot    = "@dat@"
}

Physics {
        Recombination ( SRH(DopingDep)
#                           Avalanche
#                           Band2Band
```

```
#                         NonLocal
                      )
        Mobility ( DopingDep
                   Enormal
                   HighFieldSaturation
                 )
        EffectiveIntrinsicDensity ( oldSlotboom NoFermi )
#if @< [string compare yes @DG@] >@ == 0
        eQuantumPotential
        hQuantumPotential
#endif
Noise ( Doping Traps )
}


#if @< [string compare intern @Trap@] >@ == 0
Physics (MaterialInterface="Silicon/Oxide") {
Traps(
(SingleTrap FixedCharge Conc=-1 SpaceMid=(@x0@,@y0@,@z0@))
)
}
#endif


#if @< [string compare Toxiden @Trap@] >@ == 0
Physics (Material="Oxide") {
Traps(
(SingleTrap FixedCharge Conc=-1 SpaceMid=(@x0@,@y0@,@z0@))
)
}
#endif


#if @< [string compare TSin @Trap@] >@ == 0
Physics (Material="Silicon") {
Traps(
```

```
}



(SingleTrap FixedCharge Conc=-1 SpaceMid=(@x0@,@y0@,@z0@))
)
}
#endif


Plot {
        DopingConcentration
        Potential
        eDensity hDensity
        eTemperature hTemperature
        LatticeTemperature
        eAvalanche hAvalanche
        eAlphaAvalanche hAlphaAvalanche
        ElectricField/Vector
        eMobility hMobility
        eCurrent/Vector hCurrent/Vector
        eVelocity/Vector hVelocity/Vector
        SpaceCharge
        eJouleHeat
        eQuasiFermi hQuasiFermi
        eGradQuasiFermi/Vector hGradQuasiFermi/Vector
eTrappedCharge hTrappedCharge
eInterfaceTrappedCharge hInterfaceTrappedCharge
        ConductionBandEnergy
        ValenceBandEnergy
        SRH
        Band2Band

RandomizedDoping


#if @< [string compare yes @DG@] >@ == 0
        eQuantumPotential hQuantumPotential
#endif
}
```

```
#if @< [string compare Poly @Poly_or_Elec@] >@ == 0
CurrentPlot {
        SpaceCharge(Maximum(Region="Poly1") Average(Region="Poly1")
        Minimum(Region="Poly1"))
        eDensity(Maximum(Region="Poly1") Average(Region="Poly1")
        Minimum(Region="Poly1"))
        hDensity(Maximum(Region="Poly1") Average(Region="Poly1")
        Minimum(Region="Poly1"))
        eQuasiFermi(Maximum(Region="Poly1") Average(Region="Poly1")
        Minimum(Region="Poly1"))
        hQuasiFermi(Maximum(Region="Poly1") Average(Region="Poly1")
        Minimum(Region="Poly1"))
        Potential(Maximum(Region="Poly1") Average(Region="Poly1")
        Minimum(Region="Poly1"))
#
        SpaceCharge(Maximum(Region="Poly2") Average(Region="Poly2")
        Minimum(Region="Poly2"))
        eDensity(Maximum(Region="Poly2") Average(Region="Poly2")
        Minimum(Region="Poly2"))
        hDensity(Maximum(Region="Poly2") Average(Region="Poly2")
        Minimum(Region="Poly2"))
        eQuasiFermi(Maximum(Region="Poly2") Average(Region="Poly2")
        Minimum(Region="Poly2"))
        hQuasiFermi(Maximum(Region="Poly2") Average(Region="Poly2")
        Minimum(Region="Poly2"))
        Potential(Maximum(Region="Poly2") Average(Region="Poly2")
        Minimum(Region="Poly2"))
}
#endif




}

Math {
```

```
        Method=ils
        Digits=4
        Iterations=8
        Error(circuit)=1e-20
        Error(contact)=1e-20
        Error(poisson)=1e-16
        Error(electron)=1e-10
        Error(hole)=1e-10
        Extrapolate
        Notdamped=50
        RhsMin=1e-20
        AvalDerivatives
Number_of_Threads = maximum
        Derivatives
        NoSRHPerPot
        RelErrControl
        ErrEff(Electron)=1e+6
        ErrEff(Hole)=1e+6
RandomizedVariation (
NumberOfSamples= 100
Randomize= 133707
)
}

NoisePlot {CurPotReACGreenFunction CurPotImACGreenFunction
PoPotReACGreenFunction
PoPotImACGreenFunction ReLNVXVSD ImLNVXVSD}


System {

      NMOS trans (Drain=d Source=s FGate=g Bulk=0)
      Vsource_pset vd (d 0) {dc=0.1}
      Vsource_pset vs (s 0) {dc=0}
      Vsource_pset vg (g 0) {dc=@Vmax@}
}
```

```
Solve {
Load(FilePrefix="9_Vth")
*- Creating initial guess:
ACCoupled (
            StartFrequency=0.001 EndFrequency=0.001
            NumberOfPoints=1 Decade
            Node(d s g) Exclude(vd vs vg)
ObservationNode (d g)
NoisePlot="n@node@_3D_@W@"
ACExtraction = "n@node@_3D_@W@"
ACExtract="acplot"
ACMethod=Blocked ACSubMethod("1d")=ParDiSo
                                  ){ Poisson }
}
```

Bibliography

[1] *Technology Roadmap for Semiconductors*, 2011.

[2] Gordon E. Moore, *Cramming more components onto integrated circuits*, Electronics, pp.114-117, 19 April 1965

[3] S. Inaba et al., *High performance 35 nm gate length CMOS with NO oxynitride gate dielectric and Ni salicide*, IEEE Transaction on Electron Devices, Vol. 49, No. 12, pp.2263-2270, December 2002

[4] Y. Taur, C.H. Wann and D.J. Frank, *25 nm CMOS design considerations*, in IEDM Tech. Dig., pp.789-792, 1998

[5] W. Shockley, *Problems related to p-n junctions in silicon*, Solid-State Electronics, Volume 2, pp. 35-67, January 1961.

[6] R. W. Keyes, *The Effect of Randomness in the Distribution of Impurity Atoms on FET Threshold* Applied Physics, Vol. 8, pp. 251-259, 1975.

[7] S. Borkar, *Designing reliable systems from unreliable components: the challenges of transistor variability and degradation*, IEEE Computer Society, 2005.

[8] K. Kuhn et al., *Managing Process Variation in Intel's 45nm CMOS Technology*, Intel Technology Journal, Vol. 12, 2008.

[9] K. Takeuchi, A. Nishida, T. Hiramoto, *Random Fluctuations in Scaled MOS Devices*, SISPAD 2009.

[10] H. Kim, J. Lee, J. Shin, S. Woo, H. Cho and J. Moon, *Experimental Investigation of the Impact of LWR on Sub-100-nm Device Performance*, IEEE Transaction on Electron Devices, Vol. 51, no. 12, December 2004.

[11] A. Asenov, S. Kaya and A. R. Brown, *Intrinsic Parameter Fluctuations in Decananometer MOSFETs Introduced by Gate Line Edge Roughness*, IEEE Transaction on Electron Devices, Vol. 50, no. 5, May 2003.

[12] H. Fukutome, Y. Momiyama, T. Kubo, Y. Tagawa, T. Aoyama and H. Arimoto, *Direct Evaluation of Gate Line Edge Roughness Impact on Extension Profiles in Sub-50-nm n-MOSFETs*, IEEE Transaction on Electron Devices, Vol. 53, no. 11, November 2006.

[13] A. Asenov, S. Kaya and J. H. Davies, *Intrinsic Threshold Voltage Fluctuations in Decanano MOSFETs Due to Local Oxide Thickness Variations*, IEEE Transaction on Electron Devices, Vol. 49, no. 1, January 2002.

[14] M. Koh, W. Mizubayashi, K. Iwamoto, H. Murakami, T. Ono, M. Tsuno, T. Mihara, K. Shibahara, S. Miyazaki, and M. Hirose, *Limit of Gate Oxide Thickness Scaling in MOSFETs due to Apparent Threshold Voltage Fluctuation Induced by Tunnel Leakage Current*, IEEE Transaction on Electron Devices, Vol. 48, no. 2, February 2001.

[15] V. S. Kaushik and al., *Estimation of Fixed Charge Densities in Hafnium-Silicate Gate Dielectrics*, IEEE Transaction on Electron Devices, Vol. 53, no. 10, October 2006.

[16] G. Lucovsky, *Intrinsic limitations on the performance and reliability of high-k gate dielectrics for advanced silicon devices*, IEEE International Electron Devices Meeting, IEDM Technical Digest, 2003.

[17] M. Koike et al., *Effect of HbN Bond on Pro erties of Thermally Stable Amorphous HfSiON and Applicability of this haterial to Sub-5Onm Technology Node LSIs*, IEEE International Integrated Reliability Workshop Final Report, pag. 13, October 2005.

[18] L. Capodieci, *From optical proximity correction to lithography-driven physical design (1996-2006): 10 years of resolution enhancement technology and the roadmap enablers for the next decade*, In Proceedings SPIE Volume. 6154, 615401.

[19] R. Tian, X. Tang and Wong, *Dummy-feature placement for chemical mechanical polishing uniformity in a shallow-trench isolation process*, IEEE Transactions

on Computer-Aided Design of Integrated Circuits and Systems, Volume 21, pp. 63-71, January 2002

[20] Tsang, Y.L. et al., *Modeling of the Threshold Voltage in Strained Si/Si1-x GexSi1-yGex CMOS Architectures*, IEEE Transactions on Electron Devices, Volume 54, pp.3040-3048, November 2007

[21] Al-Bayati et al., *Advanced CMOS device sensitivity to USJ processes and the required accuracy of doping and activation*, In Proceedings of the 14th International Conference on Ion Implantation Technology, pp. 185-188, September 2002.

[22] H. Fukutome, Y. Momiyama, T. Kubo, E. Yoshida, H. Morioka, M. Tajima, and T. Aoyama, *Suppression of poly-gate-induced fluctuations in carrier profiles of sub-50 nm MOSFETs* IEEE International Electron Devices Meeting, IEDM Technical Digest, pp. 1-4, December 2006

[23] K. Yokoyama, A. Yoshii, S. Horiguchi, *Threshold-Sensitivity Minimization of Short-Channel MOSFET's by Computer Simulation*, IEEE Journal of Solid-State Circuits, Vol. SC-15, no. 4, august 1980.

[24] A.R. Alvarez, L.A. Akers, *Monte Carlo analysis of sensitivity of threshold voltage in small geometry MOSFETs*, Electronics Letters, Vol. 18, no. 1, january 1982.

[25] W. Shockley, J.A. Copeland, R.P. James, *The Impedence Field Method of noise calculation in active semiconductor devices*, in *Quantum Theory of Atoms, Molecules and the Solid-State*, Per-Olov Lowdin ed., New York: Academic Press, 1966.

[26] F. Bonani, G. Ghione, M. R. Pinto, and R. K. Smith, *An Efficient Approach to Noise Analysis Through Multidimensional Physics-Based Models* IEEE Transactions on Electron Devices, Vol. 45, no. 1, January 1998

[27] F. Bonani, G. Ghione, M. R. Pinto, and R. K. Smith, *A Computationally Efficient Unified Approach to the Numerical Analysis of the Sensitivity and Noise of Semiconductor Devices* IEEE Transactions on Computer Aided Design of Integrated Circuits and Systems, Vol. 12, no. 3, March 1993

[28] K. El Sayed, A. Wettstein, S. D. Simeonov, E. Lyumkis and B. Polsky *Investigation of the Statistical Variability of Static Noise Margins of SRAM Cells Using the Statistical Impedance Field Method*, IEEE Transaction on Electron Devices, Vol. 59, n. 6, June 2012

[29] *Meshgenerator Tools guide* Synopsis Inc. , Mountain View, CA, USA.

[30] K. Takeuchi, T. Fukai, T. Tsunomura et al., *Understanding Random Threshold Voltage Fluctuation by Comparing Multiple Fabs and Technologies*, IEEE 2007.

[31] F. H. Branin, *Network sensitivity and noise analysis simplifed*, IEEE Transaction Circuit Theory, Vol. 20, pp. 285-288, 1973

[32] G. Ghione, E. Bellotti and F. Filicori, *Physical noise modelling of majority carrier devices: an adjoint network approach*, IEDM, pp. 351-355, 1989

[33] B. Honeisen and C. A. Mead, *Fundamental Limitations in Microelectronics-I, MOS Technology* Solid-State Electronics, Vol. 15, pp. 819-829, 1972.

[34] T. Hagiwara, K. Yamaguchi and S. Asai, *Threshold Voltage Deviation in very small MOS transistor due to local impurity fluctuations* in Proc. Symp. VLSI Tech. Papers, pp. 46-47, 1982.

[35] P. A. Stolk, F. P. Widdershoven and D. B. M. Klaassen, *Modeling Statistical Dopant Fluctuation in MOS Transistor* IEEE Transaction on Electron Devices, Vol. 45, no. 9, September 1998.

[36] H. S. Wong and Y. Taur, *Three-dimensional 'atomistic' simulation of discrete random dopant distribution effects in sub-0.1Î¼m MOSFETs* in IEDM Tech. Dig., pp.705-708, 1993.

[37] K. J. Kuhn, *Reducing Variation in Advanced Logic Technologies: Approaches to Process and Design for Manufacturability of Nanoscale CMOS* IEEE International Electron Devices Meeting,IEDM Technical Digest, pp. 471-474, December 2007.

[38] N. Sano, K. Matsuzawa, M. Mukai and N. Nakayama, *On discrete random dopant modeling in drift-diffusion simulations: physical meaning of 'atomistic' dopants* in Microelectronics Reliability Vol. 42 pp.189-199, 2002.

[39] K. Nishinohara, N. Shigyo and T. Wada, *Effects of microscopic fluctuations in dopant distributions on MOSFET threshold voltage*, IEEE Transaction on Electron Device, Vol.39, 1992.

[40] A. Asenov, G. Slavcheva, A. R. Brown, R. Balasubramaniam and J.H. Davies, *Statistical 3-D atomistic simulation of decanano MOSFETs*, Superlattices Microstruct 2000

[41] *Simulation of Random Dopant Fluctuation Effects in NMOSFETs*, Synopsis application note.

[42] A. Wettestein, O. Penzin, E. Lyumkis and W. Fichtner, *Random Dopant Fluctuation Modelling with the Impedance Field Method* Simulation of Semiconductor Processes and Devices, SISPAD 2003.

[43] K.S. Ralls, W.J. Skocpol, L.D. Jackel, R.E. Howard, L.A. Fetter, R.W. Epworth and D.M. Tennant, Phys. Rev. Lett., 52, 228, 1984

[44] M.J. Kirton, M.J. Uren, S. Collins, M. Schulz, A. Karmann and K. Scheffer, *Individual Defects at the* $Si - SiO_2$ *interface* Semicond. Sci. Technol., 4, 1116, 1989

[45] H.H. Mueller and M. Schulz,*Random telegraph signal: An atomic probe of the local current in field-effect transistors* J. Mater. Sci.: Mater in Electron., 6, 65, 1995

[46] G. Ghibaudo and T. Boutchacha,*Electrical noise and RTS fluctuations in advanced CMOS devices* Microelectron. Reliab., 42, 573, 2002

[47] A. Ghetti, M. Bonanomi, C. Monzio Compagnoni, A.S. Spinelli, A.L. Lacaita and A. Visconti, *P hysical Modeling of Single-Trap RTS Statistical Distribution in Flash Memories*, IEEE 46th Annual International Reliability Physics Symposium, Phoenix, 2008

[48] H. Kurata, K. Otsuga, A. Kotabe, S. Kajiyama, T. Osabe, Y. Sasago, S. Narumi, K. Tokami, S. Kamohara and O. Tsuchiya, *The impact of random telegraph signals on the scaling of multilevel Flash memories*, Proc. VLSI Circuits Symp., pp. 140â€“141, 2006

[49] N. Tega, H. Miki, Z. Ren, C. P. Dâ€™Emic, Y. Zhu, D. J. Frank, J. Cai, M. A. Guillorn, D. G. Park, W. Haensch and K. Torii, *Reduction of random telegraph noise in high-K metal-gate-stacks for 22 nm generation FETs* in Proc. IEEE IEDM, pp. 771â€“774, December 2009

[50] *Sentaurus Device User Guide* Synopsis Inc. , Mountain View, CA, USA, pag. 573-574.

[51] A. Ghetti, C. M. Compagnoni, A. S. Spinelli and A. Visconti, *Comprehensive Analysis of Random Telegraph Noise Instability and Its Scaling in Deca-Nanometer*

Flash Memories , IEEE Transaction on Electron Devices, Vol. 56, No. 8, August 2009.

[52] Y. Hori, M. Kuzuhara, Y. Ando, and M. Mizuta, *Analysis of electric field distribution in GaAs metal-semiconductor field effect transistor with a field-modulating plate*, J. Appl. Phys., vol. 87, pp. 3483-3487, Apr. 2000

[53] S. Karmalkar and U. K. Mishra *Enhancement of Breakdown Voltage in AlGaN/GaN High Electron Mobility Transistors Using a Field Plate*, IEEE Transaction on Electron Devices, Vol. 48, No. 8, August 2001

[54] F. Conti and M. Conti, *Surface breakdown in silicon planar diodes equipped with a field plate*, Solid State Electron., vol. 15, pp. 93-105, January 1972

[55] B. J. Baliga, *Trends in power semiconductor devices*, IEEE Transaction on Electron Devices, vol. 43, pp. 1717-1731, October 1996

[56] A. Gnudi, P. Ciampolini, R. Guerrieri, M. Rudan, G. Baccarani, *Sensitivity Analysis for Device Design*, IEEE Transaction on Computer-Aided Design, Vol. CAD-6, No. 5, September 1987.

[57] K. Asano, T. Miyoshi, K. Ishikura, N. Nashimoto, M. Kuzuhara, and M. Mizuta, Extended Abstracts of the 1998 International Conference on Solid State Device and Materials Hiroshima, Japan, 1998, p. 392.

[58] G. E. Bulman, V.M. Robbins, K.F. Brennan, K. Hess and G.E. Stillman, *Experimental Determination Of Impact Ionization Coefficients in GaAs* , IEEE Electron Device Letters, vol. 4, pp. 181-185, June 1983

[59] M. Bern and P. Plassmann, *Mesh generation*, in J.-R. Sack and J. Urutia, editors, Handbook of Computational Geometry. Elsevier Science, 1999

[60] S. J. Owen, *A survey of unstructured mesh generation technology*, in Proceedings of the 7th International Meshing Roundtable, pages 239-267. Sandia Nat. Lab., 1998.

[61] P.O. Persson and G. Strang, *A simple meshgenerator in Matlab*, SIAM Review, Volume 46 (2), pp. 329-345, June 2004

[62] H. Edelsbrunner, *Geometry and Topology for Mesh Generation*, Cambridge University Press, 2001.